



MOX-Report No. 13/2018

**A novel OpenSees element for single curved surface
sliding isolators**

Gandelli, E.; Penati, M.; Quaglini, V.; Lomiento, G.; Miglio, E.;
Benzoni, G.M.

MOX, Dipartimento di Matematica
Politecnico di Milano, Via Bonardi 9 - 20133 Milano (Italy)

mox-dmat@polimi.it

<http://mox.polimi.it>

A novel OpenSees element for single curved surface sliding isolators

E. Gandelli ^a, M. Penati ^b, V. Quaglini ^{a*}, G. Lomiento ^c, E. Miglio ^b, G.M. Benzoni ^d

^a *Department of Architecture, Built Environment and Construction Engineering, Politecnico di Milano, Piazza Leonardo da Vinci 32, Milano, Italy 20133*

^b *Department of Mathematics “F. Brioschi”, Politecnico di Milano, Piazza Leonardo da Vinci 32, Milano, Italy 20133*

^c *Civil Engineering Department, California State Polytechnic University, Pomona 3801 West Temple Avenue, Pomona, CA 91768*

^d *Structural Engineering, University of California San Diego, Matthews Lane, San Diego, CA 92161*

e-mail: emanuele.gandelli@polimi.it, mattia.penati@polimi.it, virginio.quaglini@polimi.it,
glomiento@cpp.edu, edie.miglio@polimi.it, benzoni@ucsd.edu

* corresponding author:

e-mail: virginio.quaglini@polimi.it

tel. +390223994248

Abstract

The increasing use of curved surface sliding bearings as seismic isolators benefits from the improvement of analytical models that can accurately capture their experimental performance and enhance the predictive capability of nonlinear response history analyses. The mathematical formulation proposed in this paper aims at addressing the variability of the coefficient of friction based on experimental data that can be retrieved from prototype tests on curved surface sliders. The formulation accounts for variation in the coefficient of friction with the instantaneous change of axial load and sliding velocity at the contact interface, and the accumulated heat due to cyclic motion; furthermore, it incorporates new features such as the static friction developed in the transition from the pre-sliding phase to the dynamic sliding condition. The proposed model has been coded in the object-oriented finite element software OpenSees by modifying the standard *SingleFPSimple3d* element that describes the force – displacement relationship of a bearing comprising one concave sliding surface and a spherical articulation. The main novelties of the new *CSSBearing_BVNC* element are inclusion of the static friction before the breakaway and degradation of kinetic friction induced by the heat developed during the motion of the articulated slider. The primary assumptions in the development of the friction model and the verification of the newly developed element are validated by agreement with available data. A case study helps to demonstrate the improved prediction capability of the new bearing element over its standard counterpart when applied to real situations, such as estimating a +50% increase in isolator displacement, superstructure drift and base shear demand under high intensity earthquakes, and possible non-activation of the sliding isolators under weak or medium intensity earthquakes.

Keywords

Curved Surface Slider; Static Coefficient of Friction; Heating Effect on Friction; OpenSees; Finite Element Bearing Element.

1. Introduction

Base isolation has been recognized as an effective means to enhance seismic protection of buildings, bridges, and power plants. Among the isolation systems developed over the past years, elastomeric and sliding bearings have emerged as the most practical and economically viable devices [1].

A crucial step in the design and implementation of seismic isolation systems is the assessment of their performance. Modern codes [2-5] have introduced the use of property modification factors, or λ factors, to account for the variation of the characteristics of isolators observed in real applications on a project-specific and product-specific basis. The main assumption behind the use of property modification factors is that in-service properties will be confined between an upper bound and a lower bound limit, partially derived from standardized prototype tests, which are linked to the design (mean) value of each property through a λ_{max} and a λ_{min} factor, respectively. The European seismic code [2] prescribes that the assessment of the upper bound (UB) and lower bound (LB) limits for each property required for the design of the isolating system should be established by evaluating the influence of the following factors: (i) aging effects including corrosion, (ii) temperature, (iii) contamination, and (iv) cumulative travel including wear. The effect of each of the above factors f_i is evaluated by comparing the maximum and minimum values of the design property, resulting from the influence of the factor f_i , to the maximum and minimum nominal values of the same property, as measured in prototype tests, and establishing the relevant $\lambda_{max,i}$ and a $\lambda_{min,i}$ factors associated with f_i . The effective UB and LB values used in the design should then be estimated from the nominal design values of the considered design property by a suitable combination of the lambda factors $\lambda_{max,i}$ and $\lambda_{min,i}$ accounting for the reduced probability of simultaneous occurrence of the maximum adverse effects of all f_i factors.

For the particular case of sliding isolators, the European standard on antiseismic devices EN 15129 [3] considers three categories of factors responsible for property variation, namely: (a) temperature and service life (cumulative travel), (b) aging, and (c) production variability. The variability associated with the first two categories is determined from the prototype tests, while for production variability a $\pm 20\%$ maximum deviation from the design value is assumed. The ratio between upper bound and lower bound values of any performance-related material property is prescribed not to exceed 1.8.

The AASHTO [4] and ASCE/SEI [5] standards, which regulate the application of seismic isolation in the United States, also account for the variability of the material performance by means of lower and upper bound analyses. For sliding systems, AASHTO [4] introduces λ factors to account for the distinct effects of temperature, aging and corrosion, velocity, accumulated travel (wear), and contamination. In its latest edition, ASCE/SEI 7-16 [5] includes a systematic procedure for

establishing upper and lower boundary values for isolator properties with consideration, in addition to aging effects and environmental conditions, and manufacturing variations, of hysteretic heating and history of loading effects, which are missing from the Eurocode [2-3]. The divergence of the isolator's properties from the mean nominal values observed during prototype testing is included in the evaluation of maximum $\lambda_{max} \leq 1.80$ and minimum $\lambda_{min} \geq 0.60$ modification factors. Eventually, in absence of experimental data, all standards [2-5] provide de facto values for likely variations due to each category of effects for use in design.

Upper and lower bound modification factors are applied to the design parameters to account for all sources of variability, allowing for the use of simplified predictive models. Bilinear constitutive models based on few parameters defined by the mechanical characteristics of the isolation unit, such as yield displacement, coefficient of friction and restoring stiffness for sliding isolators [6], or yield displacement, characteristic strength and post-elastic stiffness for lead rubber isolators [7], are commonly used. However the difficulty in determining appropriate values for the material property modification factors from experiments is one of the limitations of using bounding analysis. Sources of variability in the performance of devices addressed by the lambda factors occur in standardized tests simultaneously and can influence each other. Even during a single characterization test, the mechanical properties of a device may exhibit variations and diverge from the values used in the design [8]. As a result, the definition of an individual lambda factor for each source of variability turns out to be controversial and dependent on engineering judgment. Moreover, as the technology advances and novel materials and design solutions are introduced into modern isolators, new sources of variation are disclosed from prototype tests. Since the introduction of property modification factors, the availability of new experimental results from extensive testing programs has been constantly used to update upper and lower bound values for simplified bilinear models. As a result, a general agreement on the definition of reliable modification factors that can be safely used for the design has not yet been achieved.

A parallel effort has been conducted to formulate and validate predictive models that account for the variations of the general features of isolation devices in a practical way. Experimentally validated models can be used as an alternative to simplified models combined with λ factors, and provide an effective tool for the analysis and interpretation of experimental observations. This study deals with the formulation of a constitutive model for sliding isolators and its implementation into an object-oriented Finite Element (FE) software.

Sliding bearings with curved surfaces, either in the North-American version known as the Friction Pendulum System (FPS) [9] or in the European version called the Curved Surface Slider (CSS) bearing, are today among the most popular isolation systems in many countries worldwide [1]. In its

basic configuration (Fig. 1), the CSS bearing consists of a concave sliding plate and an articulated slider. The surface of the slider in contact with the concave plate is lined by a low-friction thermoplastic material, e.g., Polytetrafluoroethylene (PTFE) or Ultra High Molecular Weight PolyEthylene (UHMWPE), and a sliding surface is thus formed between the slider and the concave plate which accommodates the horizontal displacement of the superstructure. Improved versions of the device with multiple sliding surfaces have been proposed and used in recent years. As examples, we mention the Double Curved Surface Slider [10], capable to provide in a compact design a displacement capacity two times larger than its single surface counterpart, and the Triple Friction Pendulum [11] that exhibits an adaptive response to different hazard levels of earthquakes by changing its stiffness, effective friction and damping properties at controllable design displacements. In all cases, their mechanical behavior follows the same fundamental principles. More specifically, the number of sliding interfaces, coefficient of friction of the sliding surfaces and radius of curvature determine the bearing performance: the concave surface provides a restoring force that is proportional to the horizontal displacement, while the friction force developed during the accommodated sliding motion provides the energy dissipation capability, which reduces the transmitted lateral force and the displacement demand but increases the amount of residual displacement.

After the invention of curved surface sliders, the performance of the device was assessed by various type of tests. Preliminary prototype testing on PTFE lined isolators were aimed at investigating their effectiveness in mitigating the seismic response [12-13]. Predictive models accounting for the variation of the friction coefficient with the pressure on the PTFE liner and the sliding speed [6] were proposed, and improvements were later formulated [14] to account for the bending moments associated with unidirectional and bidirectional motion.

The variation of the coefficient of friction with velocity is commonly described in accordance with the exponential formulation [15]

$$\mu(V) = \mu_{HV} - [\mu_{HV} - \mu_{LV}] \cdot \exp(-\alpha_{dyn} \cdot |V|) \quad (1)$$

where μ_{LV} and μ_{HV} are the values of the coefficient of friction assessed at very low and very high velocity, respectively, and α_{dyn} is a parameter that regulates the rate of change of the kinetic friction coefficient with the modulus of velocity $|V|$.

The influence of the axial load N acting on the bearing can be introduced in the above formulation by expressing μ_{LV} , μ_{HV} and α_{dyn} as functions of N [6]:

$$\begin{aligned}\mu_{HV}(N) &= A_{HV} \cdot N^{(n_{HV}-1)} \\ \mu_{LV}(N) &= A_{LV} \cdot N^{(n_{LV}-1)}\end{aligned}\tag{2}$$

$$\alpha_{dyn}(N) = \alpha_0 + \alpha_1 \cdot N + \alpha_2 \cdot N^2$$

The parameters A_{LV} , A_{HV} , $n_{LV} \leq 1$, $n_{HV} \leq 1$ are constants that determine the friction coefficient models, while the parameters α_0 , α_1 , and α_2 determine the effect of the axial load on the coefficient α_{dyn} of the exponential term.

Alternatively, after observing that under some circumstances only the coefficient of friction at large velocity seems to be substantially affected from the axial load, it was proposed [16] to take μ_{LV} and α_{dyn} as constant-value parameters, and replace the first formula in Eq. (2) by the approximation

$$\mu_{HV}(p) = \mu_{HV,0} - \Delta\mu \cdot \tanh(\varepsilon \cdot p)\tag{3}$$

where p is the pressure on the contact surface of the sliding pad, $\mu_{HV,0}$ is the reference value of the high-velocity coefficient of friction at $p = 0$, and $\Delta\mu$ and ε are parameters that describe the variation of the high-velocity friction with the instantaneous pressure p on the liner material.

Past studies on full-scale sliding isolators also evidenced that friction decreases during sustained motion, and this effect is ascribed to the heating of the sliding surface consequent to energy dissipation [17-19]. As the temperature rises, the softening of the thermoplastic liner material is considered to activate a thin soft layer on the slider surface that acts as a solid lubricant and lowers the coefficient of friction. Experiments also showed that a rapid drop of the friction force occurs each time sliding takes places, e.g., at the breakaway and at any reversals of motion during unidirectional trajectories [12], due to the transition from the static to the kinetic regime. However, while the variation of kinetic friction with velocity and pressure has been recognized early on as significant and incorporated in structural analysis software such as SAP2000 [20], OpenSees [21] and 3D-BASIS-ME [22], comprehensive models accounting for the effects of heating and static friction are still not used in practice.

An integrated model that incorporates the variation of friction with pressure, velocity, and heating was recently presented by Lomiento [19]. The three sources of variation are assumed independent of each other, and within this framework, the effect of heating is reproduced by means of a variable dependent on the histories of axial load and velocity that accounts for the accumulated heat supplied to the sliding surface from energy dissipation. Kumar [23-24] proposed an alternative three-function model, wherein the reference value of the coefficient of friction μ_{ref} determined at a reference axial

bearing pressure p_0 , a reference temperature T_0 and high velocity V_0 , is adjusted to the real application by three factors k_V , k_p , and k_T that take account of the effects of instantaneous velocity, axial pressure and temperature at the sliding surface, thus

$$\mu(p, T, V) = \mu_{ref} \cdot k_p(p) \cdot k_T(T) \cdot k_V(V) \quad (4a)$$

with

$$\begin{aligned} k_p(p) &= a^{\beta(p-p_0)} \\ k_T(T) &= b(c^{\beta T} + d) \\ k_V(V) &= 1 - 0.5 \cdot \exp(-\alpha V) \end{aligned} \quad (4b,c,d)$$

where material parameters a , b , c , d , α , β are determined from experimental observations. The friction model defined by Eqs. (4a-d) has been incorporated in the “*FPBearingPTV*” element formulated in the OpenSees software [25]. However, since the direct measurement of the temperature at the sliding interface during earthquake-induced motion is not practical [17], the calibration of the temperature factor k_T requires the solution of an inverse problem, and therefore use of the model does not seem to be immediately feasible for practitioners.

The present study moves from the current state-of-the-art and aims at proposing an integrated friction model that incorporates the effects of axial load, velocity and heating, and includes new features such as the static coefficient of friction at the breakaway. First, an analytical formulation based on experimental data that can be retrieved from prototype tests is presented. This formulation is proposed as a viable tool for analyzing and interpreting the experimental results. Then the numerical formulation of the friction model is developed and incorporated in a single curved surface sliding bearing element coded in the object-oriented finite element Open Sees software. The advantages of the new OpenSees bearing element and the expected enhancement in the prediction capability of an ensuing response history analysis is discussed with reference to the case study of a reinforced concrete frame building.

2. Friction model for sliding bearings

2.1 Mathematical formulation

In the proposed model [26], the coefficient of friction of the sliding surface of the bearing is expressed as the product of two functions

$$\mu(N, V, c) = f_{NV}(N, V) \cdot f_c(c) \quad (5)$$

where $f_{NV}(N, V)$ is a first function that accounts for the effects of the instantaneous values of axial load N and velocity V , while $f_c(c)$ is a second function that accounts for the cumulated heat generated at the sliding surface through a suitable degradation variable c .

The function $f_{NV}(N, V)$ is developed upon the standard formulation recalled in Eq. (1) by introducing an additional contribution that accounts for the static friction during the sticking phase

$$f_{NV}(N, V) = \mu_{HV}(N) - [\mu_{HV}(N) - \mu_{LV}(N)] \cdot \exp(-\alpha_{dyn}|V|) + [\mu_{St}(N) - \mu_{LV}(N)] \cdot \exp(-\alpha_{St}|V|) \quad (6)$$

where μ_{St} is the static coefficient of friction, μ_{LV} and μ_{HV} are the kinetic coefficients of friction at low velocity and high velocity, respectively, α_{dyn} determines the rate of change of the kinetic coefficient of friction with the sliding velocity, and α_{St} regulates the coefficient of friction during the transition from the sticking to the sliding condition [27]. The coefficients μ_{St} , μ_{LV} and μ_{HV} in Eq. (6) depend in turn on the axial load according to power law expressions [28]

$$\begin{aligned} \mu_{HV}(N) &= A_{HV} \cdot N^{(n_{HV}-1)} \\ \mu_{LV}(N) &= A_{LV} \cdot N^{(n_{LV}-1)} \\ \mu_{St}(N) &= A_{St} \cdot N^{(n_{St}-1)} \end{aligned} \quad (7a,b,c)$$

where parameters A_{LV} , A_{HV} , $n_{LV} \leq 1$, $n_{HV} \leq 1$ have been already defined for Eq. (2), and A_{St} and $n_{St} \leq 1$ determine the effect of the axial load on the static coefficient of friction. Fig. 2 illustrates the overall variation of the friction coefficient with axial load and sliding velocity according to Eqs. (6) and (7).

The degradation function f_c defined by Eq. (8) applies to the reference coefficient of friction f_{NV} as an independent reduction factor

$$f_c(c) = \exp\left[-\left(c / c_{ref}\right)^\gamma\right] \quad (8)$$

where the c_{ref} is a parameter that regulates the rate of degradation of the coefficient of friction (e.g., the smaller the c_{ref} value, the higher the degradation), γ is a parameter that controls the shape of the function, and c is the degradation variable given by Eq. (9) and defined in Appendix A:

$$c(t) = \int_0^t N(t) \cdot |V(t)|^2 dt \quad (9)$$

By the above formulation, the change of the friction coefficient induced by heating is related to the cumulated power dissipated at the sliding surface and the distance traveled by the slider.

In the analytical model, ten parameters are required to characterize the sources of friction variation, as summarized in Table 1.

2.2 Parameter identification

Testing protocols prescribed by the European and North American standards [2-5] for sliding isolators are suitable for straightforward identification of the model parameters. The relevant tests are performed at different levels of axial load, including the design seismic load and the gravitational load. In each test, the bearing is subjected to the input of unidirectional displacement cycles with a sinusoidal waveform, performed at the design bearing displacement d_b , and fixed frequency f_0 . This way a full range of velocities from zero to the maximum velocity V_{max} is developed in the same test and the protocol covers a wide combination of loads and velocities of interest for the application.

The case of a CSS prototype tested at the SRMD Laboratory at the University of San Diego is taken as an example to show the feasibility of the procedure for parameter identification. The bearing has an effective radius $R = 6000$ mm, corresponding to an undamped oscillation period $T_{iso} = 4.91$ s, and is rated for 8000 kN vertical load and 380 mm lateral displacement.

Tests at three levels of axial load (N_1 , N_2 , and N_3), corresponding to the minimum and maximum loads acting through the isolator in earthquake conditions and to the design gravitational load, respectively, are used (Table 2).

When the force – displacement diagram from a cyclic test is analyzed (Fig. 3(a)), at any displacement d the horizontal force developed from the bearing can be expressed as the sum of two contributions, namely the hysteretic force F_μ due to friction and the restoring force F_R due to curvature

$$F = \mu \cdot N \cdot \text{sign}(V) + \frac{N}{R} d \quad (10)$$

where R is the effective radius of the bearing [29]. According to the notation used in Eq. (10), the sign of V is positive when the velocity vector is in the positive direction of the displacement axis, and negative if vice versa. The hysteretic force F_μ is calculated by subtracting the restoring force from the total force:

$$F_\mu(N, V) = \mu \cdot N \cdot \text{sign}(V) = F - \frac{N}{R} d \quad (11)$$

and hence the hysteretic force – displacement loops is derived (Fig. 3(b)).

As shown in Fig. 3, a half cycle with displacement amplitude $0.5 d_b$ and frequency $2 f_0$ is preliminarily performed before the execution of the regular cycles at the test displacement d_b . Since the temperature rise is assumed small at the early beginning of motion, and insufficient to produce a substantial change of the coefficient of friction, the force values observed in the initial half cycle are used to estimate the parameters of the friction function $f_{NV}(N, V)$.

For each load level N_i , six values of hysteretic force are sampled: the static value at the breakaway, one value at low velocity ($V < 25$ mm/s), two values in the medium velocity range ($50 \leq |V| \leq 150$ mm/s) and two values at high velocity ($V > 250$ mm/s) (Fig. 4). The coefficient of friction is calculated by dividing the modulus of the hysteretic force $|F_\mu|$ by the axial load N_i , and the obtained (V, μ) pairs are fitted by using Eq. (6), thus providing the coefficients $\mu_{HV, N_i}; \mu_{LV, N_i}; \mu_{St, N_i}; \alpha_{dyn, N_i}; \alpha_{St, N_i}$ (Fig. 5). The coefficients $\mu_{HV, N_i}, \mu_{LV, N_i}, \mu_{St, N_i}$ are plotted versus the axial load N and fitted in accordance with Eqs. (7a) to (7c) (Fig. 6), thus determining the load-effect model parameters $A_{St}, n_{St}, A_{LV}, n_{LV}, A_{HV}, n_{HV}$. The velocity-effect model parameters α_{dyn} and α_{St} , which are assumed to be independent of

the axial load, are obtained by averaging the α_{dyn, N_i} and α_{St, N_i} coefficients, i.e. $\alpha_{dyn} = \left(\sum_{i=1}^n \alpha_{dyn, N_i} \right) / n$

and $\alpha_{St} = \left(\sum_{i=1}^n \alpha_{St, N_i} \right) / n$, where $n = 3$ is the number of load levels.

The degradation function is calibrated on the three regular cycles at the test displacement d_b plus the initial half-cycle performed at each load level. First, the equivalent friction coefficient $\mu_{ED, j, i}$ and the degradation variable $c_{j, i}$ are calculated for each j -th quarter of cycle:

$$\mu_{EDj,i} = \frac{ED_{j,i}}{N_i \cdot k_j \cdot d_b} \quad (12)$$

$$c_{j,i} = \int_0^{t_j} N_i \cdot |V(t)|^2 dt \quad (13)$$

where $ED_{j,i}$ is the energy dissipated in the j -th quarter of cycle at load level N_i (i.e. the area of the j -th quarter of the force – displacement loop), d_b the test displacement, k_j is a coefficient that accounts for the actual displacement amplitude and counts 0.5 when $j = 1$ or 2, and 1.0 when $j \geq 3$, and t_j the last time instant of the j -th quarter of cycle. The obtained $(c_{j,i}, \mu_{EDj,i})$ pairs are fitted by the equation, see (Fig. 7),

$$\mu_{EDj,i} = \mu_{ED1,i} \cdot f_c(c_{j,i}) = \mu_{ED1,i} \cdot \exp\left[-(c_{j,i}/c_{ref})^\gamma\right] \quad (14)$$

where $\mu_{ED1,i}$ is the equivalent friction coefficient at the first quarter of the initial half-cycle, and load sensitive coefficients $c_{ref,i}$, γ_i are obtained. Finally, both the c_{ref} and γ parameters of the degradation

function are determined as average values on the examined n load levels, i.e. $c_{ref} = \left(\sum_{i=1}^n c_{ref,i}\right) / n$ and

$$\gamma = \left(\sum_{i=1}^n \gamma_i\right) / n.$$

By applying the procedure to the prototype of CSS isolator under consideration, the parameter values reported in Table 3 were obtained. Fig. 8 compares the hysteretic force – displacement curves calculated by using the calibrated model and the plots derived from the experiments, while in Table 4 the numerical predictions are checked against experimental data in terms of force developed at the breakaway (F_B), Energy Dissipated per Cycle (EDC) and secant stiffness (K_s), and relevant percentage errors are calculated. As shown in the figure, the analytical model is capable to predict the force increase at the breakaway and at motion reversals caused by the static friction; the small fluctuations of the experimental force observed after each transition from sticking to sliding condition are ascribed to experimental bias and inertial effects of the testing set-up rather than to actual flutter of the friction coefficient. Arrows are used to show the difference of the numerical and experimental results close to the reversals in the force – displacement loops. These discrepancies are caused by the variation (less than 10%) of the vertical load applied from the testing system to the prototype, which in turn comes from the vertical displacement of the curved surface bearing occurring at large horizontal displacement. This factor was not taken into account in the numerical analyses. The

decrease of the hysteretic force with the cumulated distance induced by heating of the sliding surface is correctly calculated by the degradation function incorporated in the friction model, with a maximum error on the *EDC* of -6.5% at the first cycle and -4.6% at the third cycle. Disregarding the test at the lowest axial load where the influence of experimental bias is larger, the maximum error on *Ks* is -4% at the first cycle and +1.2% at the third cycle. Therefore, the proposed friction model provides a reliable prediction of the force – displacement response of the Curved Surface Bearing, accounting for the variation of the coefficient of friction with axial load, velocity of sliding and heating of the surface, and including the contribution of the static friction at zero velocity.

3. Finite element model of Curved Surface Slider

The mechanical behavior of a Curved Surface Slider in two horizontal directions is a function of the geometric and material properties of the sliding surfaces, and of the axial load on the bearing.

The *SingleFPSimple3d* element is available in the finite element software OpenSees [25] to model a single Friction Pendulum™ (FP) bearing, comprised of a concave sliding surface and an articulated slider like the example in Fig. 1.

Suitable modifications were made to the source code of the current element to incorporate the friction model presented in section 2 of this paper. In this section, the assumptions involved in modeling the CSS bearing are discussed, and the verification of the code is presented.

3.1 Physical model

The physical model of the bearing is a two-node, twelve degrees of freedom, discrete element. The first node (*i*-Node) is located at the center of the concave sliding surface and the second node (*j*-Node) at the center of the spherical housing of the slider, with degrees of freedom in the global and the local coordinate systems defined as shown in Fig. 9(a).

The bearing can displace in six directions, namely, translate in the vertical and in the two horizontal directions, twist about the vertical axis, and rotate about two horizontal axes. In the vertical direction, the slider is considered rigid, but the vertical rigid-body motion of the slider accompanies the displacement in the horizontal direction.

The response of the bearing can be conveniently formulated by introducing the basic coordinate system represented in Fig. 9(b). The basic *x*-axis connects the centers of curvature of the lower and upper concave surfaces (C_i and C_j points, respectively), and basic *y*- and *z*-axes follow the right-hand rule. In such representation, the bearing has six degrees of freedom that correspond to relative displacements and rotations between the auxiliary C_i - and C_j -Nodes, and the force – deformation response can be expressed by assuming that the auxiliary nodes are connected by six springs that represent the mechanical behavior in the six basic directions of the bearing: Axial, Shear 1, Shear 2, Torsion, Rotation1, and Rotation2. The discrete spring representation has the advantages of easy implementation and of being computationally efficient [30]; structural analysis programs that allow the user to add functionalities through user-created elements, like the OpenSees software, provide a framework for such implementation.

In the basic representation the general expression of the element stiffness matrix is [25]:

$$[K_b] = \begin{bmatrix} Axial & 0 & 0 & 0 & 0 & 0 \\ 0 & Shear1 & Shea21 & 0 & 0 & 0 \\ 0 & Shear12 & Shear2 & 0 & 0 & 0 \\ 0 & 0 & 0 & Torsion & 0 & 0 \\ 0 & 0 & 0 & 0 & Rotation1 & 0 \\ 0 & 0 & 0 & 0 & 0 & Rotation2 \end{bmatrix} \quad (15)$$

and the associated element force vector

$$\{q_b\} = \begin{pmatrix} Axial \\ Shear1 \\ Shear2 \\ Torsion \\ Rotation1 \\ Rotation2 \end{pmatrix} \quad (16)$$

The *SingleFPSimple3d* element has coupled friction properties (with post-yield stiffening due to the concave sliding surface) for the shear deformations, and force-deformation behaviors defined by *UniaxialMaterial* elastic models in the remaining four directions. To capture the uplift behavior of the bearing, the user-specified *UniaxialMaterial* in the axial direction has been modified for no-tension behavior. Coupling between vertical and horizontal directions and between vertical direction and rotation is considered indirectly by using expressions for mechanical properties that are derived using explicit consideration for geometric nonlinearity due to large displacement effects [31]. By default, P-Delta moments are entirely transferred to the concave sliding surface, so that rotations of the concave sliding surface affect the shear behavior of the bearing.

3.2 Numerical formulation

The element forces, displacements, and stiffness matrices are formulated at the component level in the element's basic coordinate system and transformation matrices are used to switch from basic to local and then from local to global coordinates.

The contribution from each element is assembled in the global coordinate system to obtain the systems of equations for the whole model and solved to obtain nodal forces and displacements. The nodal response quantities calculated in the global coordinate system are transformed back to the element's local and basic coordinate systems to obtain forces

and displacements in the components. The symbols $\{u\}$ and $\{\dot{u}\}$ will be used for the nodal displacement and nodal velocity vectors, while subscripts b and l will designate the quantities in basic and local coordinates, respectively.

The software performs a numerical procedure to calculate the internal forces of the element. The description is here limited to the procedure for calculation of the two shear forces, while for the other four components the standard *UniaxialMaterial* model is adopted.

As a first step, the radii in the basic shear directions are calculated accounting for the deformation of the bearing element:

$$\begin{aligned} R_y &= \sqrt{R^2 - (u_b(3))^2} \\ R_z &= \sqrt{R^2 - (u_b(2))^2} \end{aligned} \quad (17)$$

where R is the radius of curvature of the bearing, and $u_b(2)$ and $u_b(3)$ are the displacements in the basic y and z directions defined in Fig. 9(b).

Noting that for small incremental displacements the two vectors $\{u_b\}$ and $\{\dot{u}_b\}$ have the same direction, tangent to the concave sliding surface, the absolute velocity is calculated:

$$|\dot{u}_b| = \sqrt{\left(\dot{u}_b(2) \cdot \frac{u_b(2)}{R_y} + \dot{u}_b(3) \cdot \frac{u_b(3)}{R_z}\right)^2 + (\dot{u}_b(2))^2 + (\dot{u}_b(3))^2} \quad (18)$$

The hysteretic force – displacement relationship of the Curved Surface Slider in the horizontal direction is mathematically modeled using the theory of plasticity [31-34]. When the shear force is smaller than the friction force at the sliding surface, sliding is prevented and the deformation is purely elastic. When the force exceeds the friction force, then sliding takes place.

An iterative procedure is performed to calculate shear forces and stiffnesses in basic y and z directions. At each iteration step, the normal force is first calculated

$$N = -q_b(1) + q_{b,Old}(2) \cdot \frac{u_b(2)}{R_y} + q_{b,Old}(3) \cdot \frac{u_b(3)}{R_z} - q_{b,Old}(2) \cdot u_l(6) + q_{b,Old}(3) \cdot u_l(5) \quad (19)$$

where $q_b(1)$ is the axial force calculated from the displacement component $u_b(1)$ in axial direction by applying the *UniaxialMaterial* model, and $q_{b,Old}(2)$ and $q_{b,Old}(3)$ are the values of shear force calculated at the previous iteration step.

The total resisting force in the plasticity model along each shear direction can be represented as the sum of its elastic and hysteretic force components (Fig. 10). In each direction, the stiffness associated with the elastic component is given by the ratio between the normal force and the radius

$$K2_y = \frac{N}{R_y}$$

$$K2_z = \frac{N}{R_z}$$
(20)

and the initial stiffness of the hysteretic component is given as the difference between the (isotropic) initial stiffness of the isolator, $K1$, and the elastic stiffness

$$K0_y = K1 - K2_y$$

$$K0_z = K1 - K2_z$$
(21)

The displacements of the hysteretic component are used as a state variable for the plasticity model, and the trial values of the hysteretic shear forces $qTrial(2)$ and $qTrial(3)$ are calculated as:

$$qTrial(2) = K0_y \cdot (u_b(2) - u_{b,PlasticOld}(2))$$

$$qTrial(3) = K0_z \cdot (u_b(3) - u_{b,PlasticOld}(3))$$
(22)

where $u_{b,PlasticOld}(2)$ and $u_{b,PlasticOld}(3)$ are the plastic displacements at the previous iteration step.

Since for bidirectional motion bearings with spherical surfaces exhibit isotropic behavior, a circular yield condition is adopted. A dummy parameter Y is introduced to determine transition from elastic to plastic behavior, corresponding to the transition of the bearing response from sticking to sliding conditions:

$$Y = |qTrial| - q_{yield}$$
(23)

where q_{yield} is the yield force calculated in accordance with the assumed friction model and $|q_{Trial}| = \sqrt{(q_{Trial}(2))^2 + (q_{Trial}(3))^2}$ is the resultant hysteretic shear force. Parameter Y therefore represents the excess force above the yield strength of the bearing element. Specifically,

(a) elastic step

When $Y \leq 0$ (elastic region), the shear forces are calculated as

$$\begin{aligned} q_b(2) &= q_{Trial}(2) + K_{2_y} \cdot u_b(2) - N \cdot u_l(6) \\ q_b(3) &= q_{Trial}(3) + K_{2_z} \cdot u_b(3) + N \cdot u_l(5) \end{aligned} \quad (24)$$

and the tangent stiffness for the two coupled shear directions is

$$\begin{aligned} K_b(2,2) &= K_b(3,3) = K1 \\ K_b(2,3) &= K_b(3,2) = 0 \end{aligned} \quad (25)$$

(b) plastic step

When $Y > 0$ (plastic region), the software performs a return mapping algorithm [32] to calculate the resisting force. By assuming an associative plastic flow rule, the trial slip in either shear direction is obtained by dividing the parameter Y by the initial elastic stiffness of the hysteretic component

$$\begin{aligned} dGamma_y &= Y / K0_y \\ dGamma_z &= Y / K0_z \end{aligned} \quad (26)$$

and the plastic displacement is then updated as

$$\begin{aligned} u_{b,Plastic}(2) &= u_{b,PlasticOld}(2) + dGamma_y \cdot \frac{q_{Trial}(2)}{|q_{Trial}|} \\ u_{b,Plastic}(3) &= u_{b,PlasticOld}(3) + dGamma_z \cdot \frac{q_{Trial}(3)}{|q_{Trial}|} \end{aligned} \quad (27)$$

The shear forces and the associated components of the tangent stiffness are hence calculated:

$$q_b(2) = q_{yield} \cdot \frac{q_{Trial}(2)}{|q_{Trial}|} + K_{2y} \cdot u_b(2) - N \cdot u_l(6) \quad (28)$$

$$q_b(3) = q_{yield} \cdot \frac{q_{Trial}(3)}{|q_{Trial}|} + K_{2z} \cdot u_b(3) + N \cdot u_l(5)$$

$$K_b(2,2) = K_{0y} \cdot q_{yield} \frac{q_{Trial}(3) \cdot q_{Trial}(3)}{|q_{Trial}|^3} - K_{2y}$$

$$K_b(3,3) = K_{0z} \cdot q_{yield} \frac{q_{Trial}(2) \cdot q_{Trial}(2)}{|q_{Trial}|^3} - K_{2z}$$

$$K_b(2,3) = -K_{0z} \cdot q_{yield} \frac{q_{Trial}(2) \cdot q_{Trial}(3)}{|q_{Trial}|^3} \quad (29)$$

$$K_b(3,2) = -K_{0y} \cdot q_{yield} \frac{q_{Trial}(2) \cdot q_{Trial}(3)}{|q_{Trial}|^3}$$

The procedure is run iteratively until convergence is achieved, i.e. the difference between the moduli of the resultant shear force in two consecutive runs is less than a set tolerance level. If the maximum number of iterations is exceeded, the algorithm fails and an error is returned. When convergence is achieved, the shear force components are used to formulate the element stiffness matrix in basic representation $[K_b]$ according to Eq. (29). The element stiffness matrix is then transformed into the local coordinate system and “*P-Delta*” and “*V-Delta*” moment stiffness terms are added to the local force vector. The local stiffness matrix is eventually transformed into the global coordinate system and assembled to other elements’ contributions to obtain the system of equations governing the response of the overall model.

3.3 Friction model

The standard *SingleFPSimple3d* element calculates the yield force based on the friction law coded in the associated *FrictionMaterial* model. Different friction models are available in OpenSees libraries, wherein the coefficient of friction is either a constant (*Coulomb* material) or is a function of the sliding velocity, the axial pressure or both, according to Eqs. (1) to (3).

A novel element, hereinafter called as the *CSSBearing_BVNC* element, was implemented by modifying the source code of the standard element to introduce the variation of the coefficient of friction with the degradation variable and include the static friction at the breakaway according to the formulation presented in section 2. The constitutive modeling is similar to that of the *SingleFPSimple3d* element, otherwise.

It must be noted that the absolute velocity of the bearing calculated according to Eq. (18) comprises the contribution of both elastic and plastic, i.e. sliding, deformation. Therefore, the standard OpenSees element uses the total velocity instead of the sliding velocity when calculating the coefficient of friction and this makes impossible to account, within the standard formulation, for the static coefficient of friction before sliding takes place, because the elastic velocity is never zero even during the sticking phase. To overcome this numerical issue, the incorporation of static friction was achieved in the novel formulation by introducing two distinct plastic material models for either the static or the kinetic friction with a switch condition triggered at the breakaway (Fig. 11):

$$\begin{aligned} q_{yield} &= \mu_B \cdot N & \text{for } h < 1 \\ q_{yield} &= \mu_{VNC} \cdot N & \text{for } h \geq 1 \end{aligned} \quad (30)$$

In the above, h is a variable that is incremented by one unit each time the yield condition $Y > 0$ is achieved. At the beginning of the analysis, the variable h is initialized ($h = 0$), and the yield force q_{yield} is defined by a circular yield criterion according to a *Coulomb* material, i.e. $q_{yield} = \mu_B \cdot N$, where μ_B is the static coefficient of friction at the breakaway point. At the first yielding, the variable h is updated to $h = 1$, and the plasticity algorithm switches to the user-defined *VNC_Friction* material model. The second material model calculates the yield force as $q_{yield} = \mu_{VNC} \cdot N$, where μ_{VNC} is a function of the axial load, velocity and cumulated heat flux according to the expression

$$\mu_{VNC} = \{ \mu_{HV}(N) - [\mu_{HV}(N) - \mu_{LV}(N)] \cdot \exp(-\alpha_{dyn} \cdot |\dot{u}_b|) \} \cdot \exp((-c(N, |\dot{u}_b|)/c_{ref})^\gamma) \quad (31)$$

Parameters $\mu_{HV}(N)$ and $\mu_{LV}(N)$ are calculated at each iteration step in accordance with Eqs. (7a) and (7b) based on the instantaneous values of velocity and normal force of the element given by Eqs. (18) and (19). The decrease of the coefficient of friction induced by heating is taken into account by means of a reduction factor that is calculated based on the history of the degradation variable $c(N, |\dot{u}_b|)$. At each time step, the increment Δc of the degradation variable over the time interval Δt is calculated by numerical integration of Eq. (9) according to the composite rectangle rule:

$$\Delta c(t) = N(t) \cdot |\dot{u}_b(t)|^2 \cdot \Delta t \quad (32)$$

and the variable updated as $c(t) = c(t - \Delta t) + \Delta c(t)$.

Eight friction parameters are used in the implementation of the *CSSBearing_BVNC* element, namely μ_B (static coefficient of friction), A_{LV} , A_{HV} , $n_{LV} \leq 1$, $n_{HV} \leq 1$ (load-effect parameters), α_{dyn} (velocity-effect parameter), and c_{ref} and γ (degradation parameters associated with the heating effect).

In the OpenSees software, the parameters that characterize the element response are dimensionless [25], and this requires that the units of the input parameters must be specified consistently with the units adopted for the fundamental physical quantities, in accordance with Table 5.

Different friction models, including those already coded in OpenSees, such as *Coulomb*, *VelDependent*, and *VelNormalFrcDep* materials [25], can be derived from the novel formulation by setting the relevant parameters, as shown in Table 6.

3.4 Code verification tests

Code verification of the new *CSSBearing_BVNC* element to ensure that the software produces correct results has been performed by means of a code-to-code comparison with the *SingleFPSimple3d* element.

A simple SDOF model (Fig. 12), with a $m = 100$ tons lumped mass producing a vertical force $N = 981$ kN, and connected to ground by an isolator element, is used for the tests. The isolator element has an effective radius $R = 3500$ mm and initial elastic stiffness $KI = 2.803$ kN/m. An unidirectional sinusoidal acceleration with amplitude $PGA = 0.40$ g and period $T = 1.0$ s is applied at ground level. No damping is assigned to the system.

The first step verifies the suitability of the *CSSBearing_BVNC* element to reproduce the response of the standard element coded in OpenSees software. The parameters assigned to the friction material in the new element are given in Table 7. In Test 1, the *CSSBearing_BVNC* element is

compared to the *SingleFPSimple3d* element with constant (*Coulomb*) friction coefficient $\mu = 0.10$. In Test 2, comparison is made to the *SingleFPSimple3d* element with *VelDependent* friction model and assigned parameters $\mu_{LV} = 0.05$, $\mu_{HV} = 0.15$, and $\alpha_{dyn} = 0.05$ s/mm. The resulting horizontal force – displacement curves and displacement histories are illustrated in Fig. 13 and Fig. 14, respectively. The analyses performed with either code calculate at any time instant the same values of force and displacement, as evidenced by the complete overlapping of the relevant plots. The absence of consistency errors in the new element code and its capability to reproduce conventional friction materials is therefore demonstrated.

The second step of code verification addresses the implementation of static friction and degradation effects. In Test 3, the contribution of the static coefficient of friction is introduced in the *CSSBearing_BVNC* element. The results of the analyses are illustrated in Fig. 15. The calculated force at breakaway is 297 kN, which is in perfect agreement (1% deviation) with the expected value of 294.3 kN (i.e. 0.30×981 kN). The force history is smooth with a force spike at the breakaway, and no spikes at motion reversals, demonstrating the correct switch of the yield threshold from μ_B to μ_{VNC} after the first yielding.

In Test 4, the degradation effect is introduced in the friction material by assigning the parameters

$c_{ref} = 5 \times 10^{15}$ (10^{-3} N) mm²/s and $\gamma = 1.0$, all other parameters being the same as in Test 3. Calculated force – displacement loops and response histories are illustrated in Fig. 16. The degradation of the coefficient of friction is evident from the decrease of the shear force at each cycle, which is not calculated by the standard code with *VelDependent* material (model parameters: $\mu_{LV} = 0.05$, $\mu_{HV} = 0.15$, $\alpha_{dyn} = 0.05$ s/mm); the difference in peak shear force between the two models registers -4.4% at the first cycle, and -21% at the tenth cycle. Fig. 16(d) compares for each cycle, at the instants of peak velocity, the coefficient of friction calculated from the software (red dots) to the expected value (solid line), where the degradation function f_c is analytically calculated in accordance with Eq. (8) and Eq. (9). The numerical prediction matches the analytical value with a deviation less than 0.5% at any point. It can be therefore concluded that also the incorporation of the heating effect in the new bearing element is verified.

4. Response history analysis

To numerically evaluate the *CSSBearing_BNVC* element performance and establish its potential to yield to a more accurate estimation, the newly developed code has been implemented for the dynamic analyses of a multi-degrees-of-freedom isolated structure in accordance with the provisions of the Italian Building Code [35], and the results are compared to the response calculated through the standard *SingleFPSimple3d* element [25].

4.1 Case study

The case study is a regular reinforced concrete, moment-resisting-frame building [36]. The structure has four stories at 3 m, and two bays of 5 m length in both longitudinal and lateral direction, and is supported by a rigid base slab (Fig. 17). Rectangular ($300 \times 500 \text{ mm}^2$) floor beams are supported by nine square ($400 \times 400 \text{ mm}^2$) columns. Seismic masses were evaluated by taking into account the full permanent loads plus 30% of the live loads for residential buildings [35]. The total seismic weight of each floor including the base slab is 1000 kN, resulting in a cumulative weight of the whole building of 5000 kN, and a vertical load acting on each column of 555 kN.

The structural model is implemented in the OpenSees v.2.5.4 software [25]. A moment-resisting frame structure with rigid joints is assumed in either direction of the building. *ElasticBeamColumn* elements [25] are used for the structural members, and the superstructure is considered to behave as a linear elastic system according to the provisions of the Italian Building Code [35] for base-isolated structures. The bending stiffness assigned to the columns is $K_c = 2.987 \times 10^4 \text{ N/mm}$, and a *RigidFloorDiaphragm* multi-points constraint [25] is introduced at each level to account for the in-plane stiffness of the floor slabs. The fundamental period of the superstructure is $T_{SS} = 0.324 \text{ s}$. The internal structural damping is modeled as a stiffness proportional damping [37], with parameters assigned to achieve 5% damping ratio at a 3.5 s period.

The building is isolated by means of nine bearings installed at the foundation level, one bearing underneath each column. A floor diaphragm composed by stiff beams is created above the isolation units in order to prevent differential displacements. The nodes at foundation level are constrained by means of rigid joints and subjected to the application of an *UniformExcitation* seismic input [25].

4.2 Isolation system

The isolation system comprises nine Curved Surface Sliders, with effective radius $R = 3000 \text{ mm}$, corresponding to a design period $T_{iso} = 3.47 \text{ s}$. The main geometric properties of the bearings are given in Fig. 18a. The surface of the slider in contact with the concave sliding plate has a diameter of 170 mm, resulting in an average contact pressure $p = 24.45 \text{ MPa}$ at the design seismic load of 555

kN; the slider is lined with a pad made of metal filled PTFE with a design coefficient of friction $\mu_d = 0.12$ at the design pressure [27]. The horizontal displacement capacity of the isolators is 150 mm. The *CSSBearing_BNVC* element is used to model the isolators. The parameters necessary for its implementation were identified, following the procedure outlined in section 2.2, from the prototype tests performed on a CSS bearing with similar design and same materials for the sliding surfaces [27, 38], which were scaled to match the axial load of the isolators used for the case study. Analytical curves of the coefficient of friction at three load levels are shown in Fig. 18b, and the standard force – displacement diagram of the isolator under the design seismic load is plotted in Fig. 18c.

In the response prediction studies, three friction models are compared, with parameters assigned in accordance with Table 8. The *BVNC* model defined by Eqs. (30) and (31) includes the effects of axial load, velocity, heating and static friction at breakaway. The *VNC* model based on Eq. (31) accounts for the effects of axial load, velocity and thermal degradation, but disregards the static friction. The third model denoted as *VC* model is also based on Eq. (31), but disregards the effect of axial load on the friction coefficients μ_{HV} and μ_{LV} .

Baseline references for comparison are derived from nonlinear analyses of the same structure performed by using the *SingleFPSimple3d* element with *VelDependent FrictionMaterial* [25]. Based on the experimental data for the liner material [27] and consistently with the parameters of the *VC* friction model, the following parameters have been assigned to the friction model: $\mu_{LV} = 0.04$, $\mu_{HV} = 0.12$, and $\alpha_{dyn} = 0.015$ s/mm.

4.3 Seismic inputs

The nonlinear history response analyses of the base-isolated building are performed assuming a critical structure (functional class IV [35]) with nominal life 100 years, corresponding to a reference period of 200 years, located in Lamezia Terme, South Italy (16.18° longitude, 38.58° latitude), topographic category T1, soil type A (rock or other rock-like geological formation). Target elastic spectra were determined in accordance with the Italian Building Code [35] provisions for Damage Limit State (DLS) and Collapse Prevention Limit State (CLS) earthquake hazard levels.

For either limit state, a set of seven independent unidirectional ground motions consistent with the Italian Building Code [35] was selected with REXEL v3.4 beta [39] software from the European Strong-motion Database [40]. The magnitude (M_w) of the seven ground motions was chosen within the interval (6 – 7), with epicentral distance (Rep) in the range 0-30 km. The selected waveforms were scaled to the design Peak Ground Acceleration (PGA) level of either 0.180 g (DLS level) or 0.499 g (CLS level) calculated according to the code [35]. Pertinent information on the ground motion data sets including identification of stations, fault mechanism, peak ground acceleration and velocity,

and Scale Factor are included in Tables 9 and 10. The scaled horizontal spectra at 5% damping are shown in Fig. 19 and Fig. 20. At either limit state, the average spectrum of the accelerogram set matches the Italian Building Code spectrum with a tolerance of -10/+30% in the period range 0.15 – 4.0 sec, with due consideration of the fundamental period of the base-isolation system [35].

It is noted that the vertical component of the ground motion has been neglected. Though the assumption is acknowledged unrealistic in practice, it has been adopted in order to directly compare the results of the analyses performed using the *VNC* and the *BVNC* models to the baseline results obtained through the *VelDependent* model.

4.4 Results

Preliminary to more detailed analyses, the effect of the axial load for the examined case study was assessed and found to be negligible, as shown e.g. by the close matching between the force – displacement curves calculated assuming either the *VC* or the *VNC* friction model (Fig. 21), evidencing that rocking effects of the superstructure are marginal.

Table 11 reports the levels of ground acceleration triggering the sliding bearings, which is a fundamental parameter characterizing the performance of the isolation system. Sliding takes place when the shear force through the bearings, which is the resultant of the inertial forces acting on the superstructure and the base slab masses, exceeds the frictional force at the sliding surface. At DLS level, by considering the contribution of the static coefficient of friction by means of the *BVNC* friction model, four out of the seven ground motions are unable to activate the sliding motion. An example of such behavior is given by the force – displacement loops developed under the 292x ground motion presented in Fig. 21(a). More specifically, the curves calculated using either the *VelDependent* or the *VNC* friction model denote the typical nonlinear response of sliding systems, with a post-yield branch following the elastic bearing deformation. On the contrary, when the *BVNC* friction model is used, the isolators experience only elastic deformation. At CLS level, sliding of isolators is triggered by each ground motion in the set, but the required seismic acceleration is about 3.2 times higher in the analyses performed with the *BVNC* model (1.016 m/s^2 vs. 0.317 m/s^2) in comparison to the standard friction model.

At the end of the history analyses, the response of the structure has been evaluated considering: (i) the horizontal displacement of the base slab d_{iso} ; (ii) the ratio between the overall shear force V_{iso} carried by the isolation units and the total vertical load ($N_{SS} + N_{BS}$), where N_{SS} and N_{BS} are the seismic weights of the superstructure and the base slab, respectively; (iii) the inter-story drift (Δ); (iv) the superstructure seismic coefficient (SC) defined as the ratio between the base shear V_b and the seismic weight (N_{SS}) of the superstructure; (v), the maximum floor acceleration in the superstructure a_{SS} .

During the post-processing of the analysis results, the maxima of the response parameters have been identified for each history analysis and the mean and standard deviation values calculated for each set of seven ground motion and each friction model. The results are summarized in Fig. 22 and Fig. 23.

The improvements in the accuracy of the analyses carried out by the new *CSSBearing_BNVC* element are discussed hereinafter by comparison with the results provided by the standard element with *VelDependent* friction model.

The effect of heating introduced by the *VNC* model is to reduce damping and hence to increase the displacement demand. Under the high intensity earthquakes at Collapse Prevention Limit State, a +50% increase in displacement of the base slab is calculated in comparison with the baseline response. The degradation of the coefficient of friction has a smaller influence on the shear force of the isolators (-12%), because the decrease in the hysteretic force is partially counterbalanced by the increase in the elastic force due to increased displacement, as shown e.g. by the curves in Fig. 21(b) relevant to the 5272x ground motion. The decrease in damping results also in an increase in the deformation and the internal forces in the superstructure (+18% variation in inter-story drift and base shear), while the maximum floor acceleration seems to be unaffected. At Damage Limit State no significant differences have been observed between the results of analyses computed through either the *VelDependent* or the *VNC* friction model. This is explained as a consequence of the small displacements of the isolators induced by the seismic input: since the energy dissipated as heat is proportional to the traveled displacement, under low intensity seismic shakes the energy amount may be not enough to promote a sufficient increase in temperature at the sliding surface to affect the friction coefficient.

Also the static friction accounted for in the *BNVC* model has a primary importance for determining the response of the isolation system. A possible effect of a high static coefficient of friction, as highlighted in the analyses performed at the Damage Limit State, is that for weak earthquakes with low PGA, the seismic ground acceleration can be insufficient to overcome the frictional resistance of the isolators. In such circumstances, the superstructure behaves as a fixed base structure, experiencing a substantial increase in inter-story drift and base shear (+31%), and in maximum floor acceleration (+34%) over the relevant values predicted through the *VelDependent* friction model. Although for the case study the levels of inter-story drift and shear force are within the serviceability limits [35], attention is drawn to the possible consequences of large drifts and floor accelerations on the performance of nonstructural elements [41].

At CLS level the static friction induces large increases in the shear force through the isolation system (+44%), as well as in superstructure drift and base shear (+50%), and maximum floor acceleration

(+32%) when compared to the response predicted through the *VelDependent* friction model. It must be indeed recall that until sliding of the bearings takes place, the typical structural response of a fixed base structure is observed. Though no substantial change in displacement demand is observed with respect to the response provided by the *VNC* model, a +62% increase in the isolators' shear force is calculated on average owing to the effect of the friction forces developed at breakaway in case of delayed sliding, like in the example shown in Fig. 21(c).

5. Summary and discussion

In the first part of the study, an experimentally based mathematical formulation has been presented to describe the friction behavior of curved surface sliding bearings. The formulation moves from previous theories [15, 19, 28] and introduces, as a new feature, a contribution that accounts for the increase in the coefficient of friction when the sliding velocity tends to zero. The heating effect associated with the energy dissipation at the sliding surface is modeled through a degradation function that accounts for the accumulated power of external forces and the distance traveled by the bearing, and that can be directly estimated from experimental tests without requiring impractical measurements of the temperature at the sliding surface during the motion of the isolator. The degradation variable is in fact determined based on mechanical quantities, such as the axial force and the sliding velocity.

The application to one bearing tested at the SRMD Test Facility at the University of California has been presented to demonstrate the ease of the procedure for parameter identification. The model parameters are obtained from the prototype tests prescribed by the standards to assess the performance of the isolators. Since these tests are already compulsory for the manufacturer, additional tests are not required. Though the model parameters were obtained by using a simple least-square fitting procedure, the force – displacement loops calculated through the calibrated model provided close agreement with the experimental curves. Nevertheless, the development of a refined calibration procedure is in progress, and will be presented in a future improvement.

The friction model has been implemented in the *CCSBearing_BVNC* element formulated in OpenSees software by modifying the source code of the standard *SingleFPSimple3d* element [25]. The *SingleFPSimple3d* element describes the force – displacement relationship of a bearing comprising one concave sliding surface and a spherical articulation, but in principle the formulation can be extended to any number of curved surfaces.

Since the new element modifies only the friction model that is used to calculate the shear force of the bearing, while the constitutive modeling is similar to the *SingleFPSimple3d* element otherwise, code verification was focused on the new features, i.e., the switching from the static friction represented by a Coulomb model to the kinetic friction model after the breakaway, and the degradation effect. Finally, an application of the *CCSBearing_BVNC* element in the history response analysis of a real building has been presented. The analyses were conducted in accordance with the Italian Building Code [35], assuming two earthquake hazard levels, and a set of seven recorded ground motion for each level. The *CCSBearing_BVNC* element reasonably simulates the typical force – displacement relationships of sliding bearings with curved surfaces and evidences the two effects of force increase at breakaway and degradation of the friction coefficient during sustained motion, thereby confirming

the improved estimation capability over the standard element. In particular, at Collapse Prevention Limit State (CLS) accounting for the degradation of the coefficient of friction produces a +50% increase in displacement demand over the standard element, while accounting for the static friction produces a +42% increase in shear force through the isolation system, a +50% increase in the superstructure drift and base shear, and a +32% increase in acceleration. Moreover, the analyses show that depending on the ground motion characteristics, a high value of the static coefficient of friction can prevent the activation of the sliding isolators under weak or medium intensity earthquakes with short return period, like at the Damage Limit State (DLS).

The static friction is demonstrated to be a fundamental parameter affecting the overall response of the isolation system, because when a high static friction force prevents sliding, the isolation system remains in the sticking condition, and the superstructure demonstrates the response of a non-isolated structure. Since current bearing elements coded in software programs for structural analysis do not incorporate the static friction contribution, this can lead to underestimate the forces and accelerations induced in the superstructure, especially in cases where the static coefficient of friction is significantly higher than the low-velocity coefficient μ_{LV} . The proposed *CSSBearing_BVNC* element is expected to overcome this issue.

Only the static friction before the breakaway has been taken into account in the *CSSBearing_BVNC* element, in order to keep the numerical code simple, whereas friction spikes at motion reversals, and at any temporary stop when the velocity goes to zero are disregarded. The static friction at motion reversal is in general lower than at the breakaway, and experimental work demonstrated that for PTFE – stainless steel interfaces commonly used in sliding bearings the breakaway friction disappears after just one cycle of loading [12-13]; therefore the approximation is deemed acceptable. However it is acknowledged that the “*CSSBearing_BVNC*” element cannot be used to represent the behavior of sliding bearings exhibiting the stick-slip phenomenon, i.e. a spontaneous jerking motion consisting of alternating motion and arrest that is the consequence of a lower friction force for a higher sliding velocity, i.e. a substantially higher static than kinetic friction [42].

In a future development, the “*CSSBearing_BVNC*” element will be challenged by comparing the numerical analyses to results of bidirectional shaking table tests of base-isolated building mock-ups, in order to validate the viability of the parameter identification based on unidirectional tests. During a ground shaking the motion is multidirectional and a consequent lower heat flux and friction degradation than during unidirectional motion is expected [19]. It must be indeed noted that, though the proper calibration of the degradation effect developed during a multidirectional motion requires a specific experimental investigation, an adaptation of the friction model extrapolated from the unidirectional formulation to bidirectional situations has been formulated in the numerical model,

where the absolute velocity across the isolator is expressed by the norm of the vector $|\dot{u}_b|$ and used in Eq. (32) to calculate the increment of the degradation variable $c(t)$.

Although the current presentation is confined to single curved surface isolators owing to their inherent simplicity, the model can be applied to multiple curved surface bearings by modifying the existing *TripleFrictionPendulum* element in the OpenSees software [25]. According to the approach presented in Section 3 for single curved surface bearings, at each surface of the triple pendulum the associated plasticity model can be determined by two yield thresholds and a switch condition equivalently to Eq. (30), whereas the constitutive modeling is similar to the existing *TripleFrictionPendulum* element otherwise. In case of multiple surfaces, a different set of parameters can be assigned to each surface in order to account for different material combinations and friction characteristics.

6. Conclusions

- (1) An experimentally-based mathematical formulation describing the friction behavior of curved surface sliding bearings has been presented. The novel features introduced by the formulation are the contribution of the static friction during the sticking phase and the degradation of the coefficient of friction induced by the heat generated during the sliding motion, whereas the dependence of the friction coefficient on the instantaneous values of axial load and sliding velocity follows accepted practice within the literature.
- (2) A total number of 10 parameters are used to represent the sources of variation. The parameters needed for the implementation of the model can be determined directly from the unidirectional prototype tests prescribed by the standards and already compulsory for the manufacturers. A practical application to a real curved surface bearing, demonstrating the ease of the procedure of parameter identification, is presented in the paper.
- (3) The new *CSSBearing_BVNC* element is formulated in the object-oriented OpenSees software by modifying the standard *SingleFPSimple3d* element to include the proposed friction model. The consistency of the new element has been verified in a code-to-code comparison by means of numerical tests considering unidirectional histories.
- (4) A comparative evaluation performed through a case study highlights the potential of the newly developed isolator element to yield a more accurate estimation. Nonlinear response history analyses of a base-isolated building help to quantify the improved prediction capability over the standard element when applied to real situations, with a +50% increase in estimate of displacement demand, superstructure drift and shear force at Collapse Prevention Limit State, and possible non-activation of the sliding isolators due to level of actual static friction under weak or medium intensity earthquakes at Damage Limit State.

Further studies should extend the verification process to bidirectional load trajectories, and present an experimental validation by simulating actual experimental observations.

Funding

This work was supported by the Italian Department of Civil Protection (DPC) within the ReLUIS/DPC 2014-2018 research program.

References

- [1] Martelli A, Clemente P, De Stefano A, Forni M, Salvatori A. Recent development and application of seismic isolation and energy dissipation and conditions for their correct use. In: Ansal A, editor. Perspectives on European Earthquake Engineering and Seismology. Volume 1; New York: Springer; 2014, p. 449-88.
- [2] EN 1998-2. Eurocode 8: Design of structures for earthquake resistance – Part 2: Bridges, Brussels: European Committee for Standardization; 2005.
- [3] EN 15129. Antiseismic devices. Brussels: European Committee for Standardization; 2009.
- [4] AASHTO Guide specifications for seismic isolation design. 4th ed. Washington: American Association of State Highway and Transportation Officials; 2014.
- [5] ASCE/SEI 7-16. Minimum Design Loads and Associated Criteria for Buildings and Other Structures, Reston: American Society of Civil Engineers; 2016.
- [6] Constantinou M, Mokha A, Reinhorn A. (1990): Teflon bearings in base isolation II: Modeling. *J Struct Eng (ASCE)* 1990;116:455-74. [http://dx.doi.org/10.1061/\(ASCE\)0733-9445\(1990\)116:2\(455\)#sthash.iuM3Yorl.dpuf](http://dx.doi.org/10.1061/(ASCE)0733-9445(1990)116:2(455)#sthash.iuM3Yorl.dpuf).
- [7] Robinson WH. Lead-rubber hysteretic bearings suitable for protecting structures during earthquakes. *Earthq Eng Struct Dyn* 1982;10:593-604. <http://dx.doi.org/10.1002/eqe.4290100408>.
- [8] Benzoni G, Lomiento G, Bonessio N. Testing protocols for seismic isolation systems. In: Proceedings of XIV ANIDIS Conference, Bari, Italy; 2011.
- [9] Zayas VA, Low SS, Mahin SA. The FPS earthquake protection system: Experimental report. Report No. UCB/EERC-87/01, Pacific Earthquake Engineering Research Center, University of California at Berkeley; 1987.
- [10] Fenz DM, Constantinou MC. Behavior of the double concave Friction Pendulum bearing. *Earthquake Earthq Eng Struct Dyn* 2006;35: pp. 1403–24, <http://dx.doi.org/10.1002/eqe.589>.
- [11] Sarlis AA, Constantinou MC, Reinhorn AM. Shake table testing of Triple Friction Pendulum Isolators under extreme conditions. Technical Report NCEER-13-0011, National Center for Earthquake Engineering Research, 2013.
- [12] Mokha A, Constantinou MC, Reinhorn AM. Teflon bearings in base isolation I: Testing. *J Struct Eng (ASCE)* 1990;116:438–544. [http://dx.doi.org/10.1061/\(ASCE\)0733-9445\(1990\)116:2\(438\)](http://dx.doi.org/10.1061/(ASCE)0733-9445(1990)116:2(438)).

- [13] Mokha A, Constantinou MC, Reinhorn AM, Zayas VA. Experimental study of friction-pendulum isolation system. *J Struct Eng (ASCE)* 1991;117:1201-17. [http://dx.doi.org/10.1061/\(ASCE\)0733-9445\(1991\)117:4\(1201\)](http://dx.doi.org/10.1061/(ASCE)0733-9445(1991)117:4(1201)).
- [14] Tsai CS. Finite element formulations for friction pendulum seismic isolation bearings. *Int J Numer Meth Engng* 1997;40:29–49. [http://dx.doi.org/10.1002/\(SICI\)1097-0207\(19970115\)40:1<29::AID-NME47>3.0.CO;2-A](http://dx.doi.org/10.1002/(SICI)1097-0207(19970115)40:1<29::AID-NME47>3.0.CO;2-A).
- [15] Constantinou MC, Tsoelas P, Kasalanati A, Wolff ED. Property Modification Factors for Seismic Isolation Bearings. Report MCEER-99-0012, State University of New York at Buffalo; 1999.
- [16] Tsoelas P, Constantinou MC, Kim YS, Okamoto S. Experimental study of FPS system in bridge seismic isolation. *Earthq Eng Struct Dyn* 1996;25:65-78. [http://dx.doi.org/10.1002/\(SICI\)1096-9845\(199601\)25:1<65::AID-EQE536>3.0.CO;2-A/pdf](http://dx.doi.org/10.1002/(SICI)1096-9845(199601)25:1<65::AID-EQE536>3.0.CO;2-A/pdf).
- [17] Constantinou MC, Whittaker AS, Kalpakidis Y, Fenz DM, Warn GP. Performance of seismic isolation hardware under service and seismic loading. Report MCEER-07-0012, Multidisciplinary Center for Earthquake Engineering Research, State University of New York at Buffalo; 2007.
- [18] Lomiento G, Bonessio N, Benzoni G. Concave sliding isolator's performance under multi-directional excitation. *Int J Earthq Eng* 2013;3:17-32.
- [19] Lomiento G, Bonessio N, Benzoni G. Friction Model for Sliding Bearings under Seismic Excitation. *J Earthq Eng* 2013;17:1162-91. <http://dx.doi.org/10.1080/13632469.2013.814611>, 1162-1191.
- [20] CSI Analysis Reference Manual For SAP2000®, ETABS®, SAFE® and CSiBridge, Berkeley: Computers and Structures Incorporated (CSI); 2016.
- [21] McKenna F, Fenves G, Scott M. Computer program OpenSees: open system for earthquake engineering simulation, Pacific Earthquake Engineering Research Center, University of California at Berkeley; 2006. <http://opensees.berkeley.edu> [accessed 17.04.30].
- [22] Tsoelas PC, Constantinou MC, Reinhorn AM. 3D-BASIS-ME: Computer program for nonlinear dynamic analysis of seismically isolated single and multiple structures and liquid storage tanks. Report NCEER-94-0010, National Center for Earthquake Engineering Research, State University of New York at Buffalo; 1994.

- [23] Kumar M, Whittaker AS, Constantinou MC. Characterizing friction in sliding isolation bearings. *Earthq Eng Struct Dyn* 2015;44:1409-25. <http://dx.doi.org/10.1002/eqe.2524>.
- [24] Kumar M, Whittaker AS, Constantinou M.C. Seismic isolation of nuclear power plants using sliding bearings. Report MCEER-15-0006, Multidisciplinary Center for Earthquake Engineering Research, State University of New York at Buffalo; 2015.
- [25] OpenSees Manual, http://opensees.berkeley.edu/wiki/index.php/Main_Page; 2017 [accessed 17.04.30].
- [26] Gandelli E. Advanced tools for the design of sliding isolation systems for seismic-retrofitting of hospitals, PhD dissertation, Politecnico di Milano; 2017.
- [27] Quaglini V, Bocciarelli M, Gandelli E, Dubini P. Numerical assessment of frictional heating in sliding bearings for seismic isolation. *J Earthq Eng* 2014;18:1198-216. <http://dx.doi.org/10.1080/13632469.2014.924890>.
- [28] Bowden FP, Tabor D. The friction and lubrication of solids – part II. London: Oxford University Press; 1964.
- [29] Al-Hussaini TM, Zayas VA, Constantinou MC. Seismic isolation of a multi-story frame structure using spherical sliding isolation systems, Report No. NCEER-94-0007, National Center for Earthquake Engineering Research, State University of New York at Buffalo; 1994.
- [30] Kumar M, Whittaker AS, Constantinou MC. An advanced numerical model of elastomeric seismic isolation bearings. *Earthq Eng Struct Dyn* 2014;43:1955–74. <http://dx.doi.org/10.1002/eqe.2431>.
- [31] Mosqueda G, Whittaker AS, Fenves GL, Mahin SA. Experimental and analytical studies of the Friction Pendulum system for the seismic protection of bridges, Report No. UCB/EERC-2004/01, Pacific Earthquake Engineering Research Center, University of California at Berkeley; 2004.
- [32] Simo JC, Hughes TJR. Computational inelasticity. New York: Springer; 1998.
- [33] Sivaselvan MV, Reinhorn AM. Nonlinear structural analysis towards collapse simulation: a dynamical systems approach. Report No. MCEER-2004-05, Multidisciplinary Center for Earthquake Engineering Research, State University of New York at Buffalo; 2004.
- [34] Ray T. Modeling of multi-dimensional inelastic and nonlinear elastic structural systems. PhD dissertation, State University of New York at Buffalo; 2013.

- [35] NTC. Norme Tecniche per le Costruzioni, Decreto Ministeriale 14/01/2008, Rome (in italian), 2008.
- [36] Lomiento G, Bonessio N, Okten MS, Benzoni G. Effect of frictional characteristics on the response of sliding base-isolated buildings under three components of earthquake excitation. In: Proceedings of 14th World Conference on Seismic Isolation, Energy Dissipation and Active Vibration Control of Structures (14WCSI), San Diego, CA; 2015.
- [37] Ryan KL, Polanco J. Problems with Rayleigh damping in base-isolated buildings. *J Struct Eng* 2008;134:1780-84. [http://ascelibrary.org/doi/pdf/10.1061/\(ASCE\)0733-9445\(2008\)134:11\(1780\)](http://ascelibrary.org/doi/pdf/10.1061/(ASCE)0733-9445(2008)134:11(1780)).
- [38] Quaglini V. High damping curved surface sliding isolators for bridges. In: Biondini F, Frangopol DM, editors. *Bridge Maintenance, Safety, Management, Resilience and Sustainability*. Boca Raton: CRC Press; 2012.
- [39] Iervolino I, Galasso C, Cosenza E. REXEL: computer aided record selection for code-based seismic structural analysis. *Bull Earthq Eng* 2010;8:339–62. <http://dx.doi.org/10.1007/s10518-009-9146-1>.
- [40] Ambraseys N, Smit P, Sigbjornsson R, Suhadolc P, Margaris B. Internet-Site for European Strong-Motion Data, European Commission, Research-Directorate General, Environment and Climate Programme, <http://www.isesd.cv.ic.ac.uk/ESD/>; 2002 [accessed 17.04.30].
- [41] Filiatrault A, Sullivan T. Performance-based seismic design of nonstructural building components: The next frontier of earthquake engineering. *Earthq. Eng. Eng. Vib.* 2014;13:17-46. <http://doi.org/10.1007/s11803-014-0238-9>.
- [42] Bowden FP, Leben L. The nature of sliding and the analysis of friction. *Proc. Royal Soc. Lond.* 1939;169A:371-9. <http://dx.doi.org/10.1098/rspa.1939.0004>.

APPENDIX A

The definition of the degradation variable starts from the original work by Lomiento [19], whom the interested reader is referred to for more details.

The temperature rise at the contact area between the slider and the concave surface of the sliding bearing depends on the heat flux generated by the frictional force, equal to the power dissipated per unit area. Assuming that the dissipated energy is completely converted into heat, the heat flux q is expressed as

$$q = \frac{\mu N |V|}{\pi b^2} \quad (\text{A1})$$

where μ , N and V represent the instantaneous values of coefficient of friction, applied load and velocity of sliding at the surface, respectively, and b is the radius of the contact surface of the slider, which determines the size of the heat source. This heat flux varies in intensity and position during the sliding motion, nevertheless for short duration motion the temperature rise on the surface is directly related to the cumulative heat flux acting on the surface from the beginning of the sliding motion.

During the time interval dt , the heat source moves from the position u to the position $u + du$, distributing its heat flux over the gray surface with area $2b \cdot du$ shown in Fig. A1.

Neglecting the second-order terms, the concave sliding surface is subjected, during each time interval dt , to an equivalent heat flux that is assumed uniformly distributed over the whole surface of radius B , given by:

$$d\bar{q} = \frac{\mu N |V|}{\pi b^2} \cdot \frac{2b \cdot du}{\pi B^2} = \frac{2\mu \cdot N \cdot V^2 dt}{\pi^2 b B^2} \quad (\text{A2})$$

with $du = |V| dt$. In writing Eq. (A2) the radius of curvature is assumed to be sufficiently large that the actual area of the concave sliding surface can be replaced by the area $\pi^2 B^2$ of its projection over the horizontal plane.

The uniformly distributed heat flux developed during the time interval $(t_0 - t)$ can be cumulated as:

$$\bar{q}(t) = \frac{2}{\pi^2 b B^2} \int_{t_0}^t \mu \cdot N \cdot V^2 dt \quad (\text{A3})$$

By elimination of the μ term from Eq. (A3), a new variable $c'(t)$, with dimension of a heat flux (i.e., power per unit area), is defined as:

$$c'(t) = \frac{2}{\pi^2 b B^2} \int_{t_0}^t N \cdot V^2 dt \quad (\text{A4})$$

where N , V , b , and B have been previously defined.

A suitable expression for the degradation function proposed in the referred study [19] is :

$$f_c(c') = \exp\left[-(c' / c'_{ref})^\gamma\right] \quad (\text{A5})$$

where the constant c'_{ref} accounts for the rate of degradation of the coefficient of friction with the cycling variable (a smaller value of c'_{ref} means faster degradation) and the exponent γ controls the shape of the function. The values of c'_{ref} and γ could be obtained by least square regression analysis of the experimental results.

A further simplification can be introduced by multiplying both $c'(t)$ and c'_{ref} by the geometric quantity $2/(\pi^2 b B^2)$, resulting in the new variable $c(t)$:

$$c(t) = c'(t) \cdot \frac{\pi^2 \cdot b \cdot B^2}{2} = \int_{t_0}^t N \cdot V^2 dt \quad (\text{A6})$$

and the new constant c_{ref} :

$$c_{ref} = c'_{ref} \cdot \frac{\pi^2 \cdot b \cdot B^2}{2} \quad (\text{A7})$$

Since for isolators with same sliding materials and different geometry, c'_{ref} is directly proportional to the geometric quantity $2/(\pi^2 b B^2)$ [19], the new constant c_{ref} turns out to be independent of the geometry of the device.

The variable $c(t)$ defined in (A6) corresponds to the degradation variable assumed in the study and expressed by Eq. (9). The variable has dimension of Force \times Length² / Time, and, if the coefficient of friction were to be kept within the integral of Eq. (A6), then $c(t)$ would represent the integral of power dissipation over the trajectory of the slider, which is

proportional, through a geometrical quantity, to the cumulative heat flux distributed to the concave sliding surface during the time interval $t_0 - t$.

The use of $c'(t)$ and $c(t)$ to represent the heating effect over the sliding surface implies the hypothesis of uniform distribution of the heat flux, i.e. it disregards the above mentioned existence of higher heat fluxes in the areas interested by more frequent sliding activity. In the reference study [19] a refined cyclic variable accounting for non-uniform temperature distribution over the surface (higher temperatures are reached in regions where sliding motion occurs more frequently) was also investigated. The relevant analyses showed that the variation of temperature over the surface affects mainly the local behavior of the isolator while a global performance parameter such as the Energy Dissipated per Cycle is more affected by the average temperature, thereby indicating the variable $c'(t)$ defined by Eq. (A4), and consequently $c(t)$, as suitable for practical applications.

Table 1. Parameters of the analytical friction model

source of variation	parameters
load	$A_{LV}, A_{HV}, A_{St}, n_{LV}, n_{HV}, n_{St}$
velocity	$\alpha_{dyn}, \alpha_{St}$
heating	c_{ref}, γ

Table 2. Test conditions for parameter identification of a 8000 kN isolator with 380 mm design displacement and fundamental period $T_{iso} = 4.91$ s

test	N (kN)	d_b (mm)	V_{max} (mm/s)	f_0 (Hz)	shape	cycles (#)
1	2500	380	486	0.2035	sine	3
2	5000	380	486	0.2035	sine	3
3	8000	380	486	0.2035	sine	3

N : axial load; d_b : displacement amplitude; V_{max} : peak velocity; f_0 : frequency

Table 3. Model parameters calibrated for the examined CSS isolator

source of variation	parameter	unit
load	$A_{LV} = 11.27$	$\text{kN}^{(1-n_{LV})}$
	$n_{LV} = 0.37$	–
	$A_{HV} = 9.65$	$\text{kN}^{(1-n_{HV})}$
	$n_{HV} = 0.46$	–
	$A_{St} = 3.51$	$\text{kN}^{(1-n_{St})}$
	$n_{St} = 0.60$	–
velocity	$\alpha_{dyn} = 0.035$	s/mm
	$\alpha_{St} = 0.35$	s/mm
heating	$c_{ref} = 4 \times 10^{10}$	$\text{kN mm}^2/\text{s}$
	$\gamma = 0.60$	–

Table 4. Numerical predictions vs. experimental results and percentage error of the proposed model

test	cycle #	F_B (kN)			EDC (kJ)			K_s (kN/m)		
		experimental	model	error (%)	experimental	model	error (%)	experimental	model	error (%)
test 1	1	406.1	395.9	-2.5	495.67	495.66	0.0	1233.4	1308.1	6.1
	2	=	=		456.71	455.09	-0.4	1154.1	1239.3	7.4
	3	=	=		433.23	425.78	-1.7	1112.4	1190.8	7.0
test 2	1	586.5	593.3	1.2	679.89	635.55	-6.5	2065.6	1983.9	-4.0
	2	=	=		584.20	560.39	-4.1	1861.3	1851.6	-0.5
	3	=	=		529.99	508.80	-4.0	1741.6	1762.0	1.2
test 3	1	756.4	768.5	1.6	784.80	738.78	-5.9	2765.7	2676.6	-3.2
	2	=	=		654.30	627.34	-4.1	2508.4	2477.0	-1.3
	3	=	=		580.21	553.73	-4.6	2360.3	2345.5	-0.6

F_B : Force at the breakaway; EDC : Energy Dissipated per Cycle; K_s : secant stiffness calculated between $-0.95d_b$ and $+0.95d_b$

Table 5. Units of the friction parameters of the *CSSBearing_BVNC* element

parameter	Unit
μ_B	–
α_{dyn}	s/mm
A_{LV}	$(10^{-3} \text{ N})^{(1-n_{LV})}$
n_{LV}	–
A_{HV}	$(10^{-3} \text{ N})^{(1-n_{HV})}$
n_{HV}	–
c_{ref}	$(10^{-3} \text{ N}) \text{ mm}^2/\text{s}$
γ	–

Table 6. Friction models enveloped by the *CSSBearing_BVNC* element and equivalent *FrictionMaterial* models coded in OpenSees software

source of variation	OpenSees <i>FrictionMaterial</i>	parameter set
load, velocity, heating	=	$\mu_B = A_{LV}$ all other parameters assigned
load, velocity,	<i>VelNormalFrcDep</i>	$\mu_B = A_{LV}$ $c_{ref} = 10^{100}$, $\gamma = 1$ all other parameters assigned
velocity	<i>VelDependent</i>	$\mu_B = A_{LV}$ $n_{LV} = n_{HV} = 1$ $c_{ref} = 10^{100}$, $\gamma = 1$ all other parameters assigned
constant friction	<i>Coulomb</i>	μ_B assigned $A_{LV} = A_{HV} = \mu_B$ $n_{LV} = n_{HV} = 1$ $\alpha_{dyn} = 10^{100}$ $c_{ref} = 10^{100}$, $\gamma = 1$

Table 7. Friction model parameters assigned in code verification tests

parameter	unit	Test 1	Test 2	Test 3	Test 4
μ_B	–	0.10	0.05	0.30	0.30
α_{dyn}	s/mm	10^{100}	0.005	0.005	0.005
A_{LV}	$(10^{-3} \text{ N})^{(1-n_{LV})}$	0.10	0.05	0.05	0.05
n_{LV}	–	1	1	1	1
A_{HV}	$(10^{-3} \text{ N})^{(1-n_{HV})}$	0.10	0.15	0.15	0.15
n_{HV}	–	1	1	1	1
c_{ref}	$(10^{-3} \text{ N}) \text{ mm}^2/\text{s}$	10^{100}	10^{100}	10^{100}	5×10^{15}
γ	–	1	1	1	1

Table 8. Friction model parameters assigned in nonlinear response analyses of the case study

parameter	unit	friction model		
		<i>VC</i>	<i>VNC</i>	<i>BVNC</i>
μ_B	–	0.04	0.04	0.165
α_{dyn}	s/mm	0.015	0.015	0.015
A_{LV}	$(10^{-3} \text{ N})^{(1-n_{LV})}$	0.04	195.953	195.953
n_{LV}	–	1	0.578	0.578
A_{HV}	$(10^{-3} \text{ N})^{(1-n_{HV})}$	0.12	4228.765	4228.765
n_{HV}	–	1	0.480	0.480
C_{ref}	$(10^{-3} \text{ N}) \text{ mm}^2/\text{s}$	3.49×10^{14}	3.49×10^{14}	3.49×10^{14}
γ	–	0.40	0.40	0.40

Table 9. Accelerogram dataset for analyses at Damage Limit State

Record	Waveform	Earth quake	Station	Fault mechanism	Date [mm/dd/yy]	Mw [-]	Rep [-]	PGA [m/s²]	PGV [m/s]	SF
Bingol	7142y	2309	ST539	strike slip	5/1/2003	6.3	14	2.9178	0.2097	0.6086
Campano Lucano	292x	146	ST98	normal	11/23/1980	6.9	25	0.5878	0.0436	3.0214
Mt. Vatnafjoll	5272x	1338	ST2487	oblique	5/25/1987	6	24	0.3222	0.0168	5.5123
Friuli	55x	34	ST20	thrust	5/6/1976	6.5	23	3.4985	0.2061	0.5076
South Iceland (aftershock)	6335y	2142	ST2557	strike slip	6/21/2000	6.4	15	1.1322	0.1083	1.5685
Mt. Vatnafjoll	5270x	1338	ST2486	oblique	5/25/1987	6	25	0.3021	0.0279	5.8789
Golbasi	410y	189	ST161	oblique	5/5/1986	6	29	0.5380	0.0749	3.3007
mean						6.3	22.14	1.3283	0.098186	2.914

Mw: magnitude; Rep: epicentral distance; PGA: Peak Ground Acceleration (not scaled); PGV: Peak Ground Velocity (not scaled); SF: Scale Factor

Table 10. Accelerogram dataset for analyses at Collapse Prevention Limit State

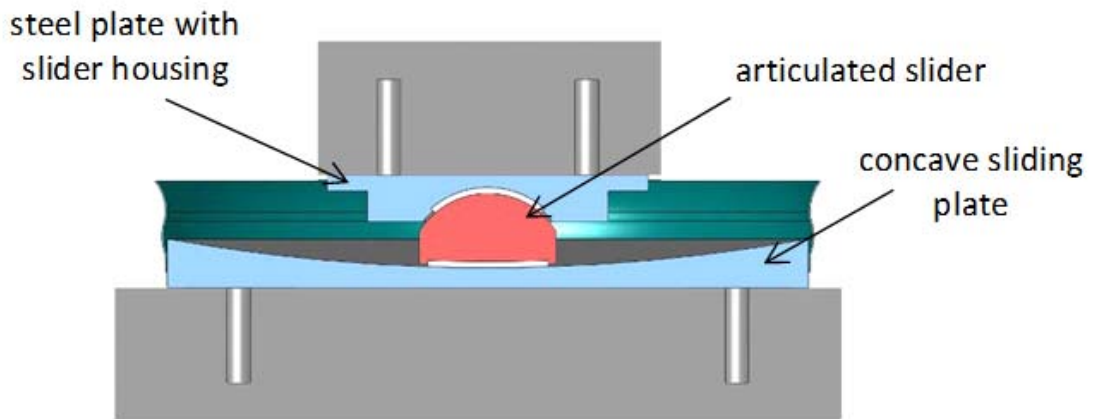
Record	Waveform	Earth quake	Station	Fault mechanism	Date [mm/dd/yy]	Mw [-]	Rep [-]	PGA [m/s²]	PGV [m/s]	SF
Campano Lucano	292x	146	ST98	normal	11/23/1980	6.9	25	0.5878	0.0436	8.8362
Campano Lucano	292y	146	ST98	normal	11/23/1980	6.9	25	0.5876	0.0585	8.8362
Montenegro	198x	93	ST64	thrust	4/15/1979	6.9	21	1.7743	0.1705	2.7582
South Iceland (aftershock)	6335x	2142	ST2557	strike slip	6/21/2000	6.4	15	1.2481	0.1659	3.9211
South Iceland	4675x	1635	ST2487	strike slip	6/17/2000	6.5	13	1.2916	0.1611	3.7890
Bingol	7142x	2309	ST539	strike slip	5/1/2003	6.3	14	5.0514	0.336	0.9688
Campano Lucano	294y	146	ST100	normal	11/23/1980	6.9	26	0.7783	0.146	6.2888
mean						6.7	19.85	1.6170	0.1545	4.9115

Mw: magnitude; Rep: epicentral distance; PGA: Peak Ground Acceleration (not scaled); PGV: Peak Ground Velocity (not scaled); SF: Scale Factor

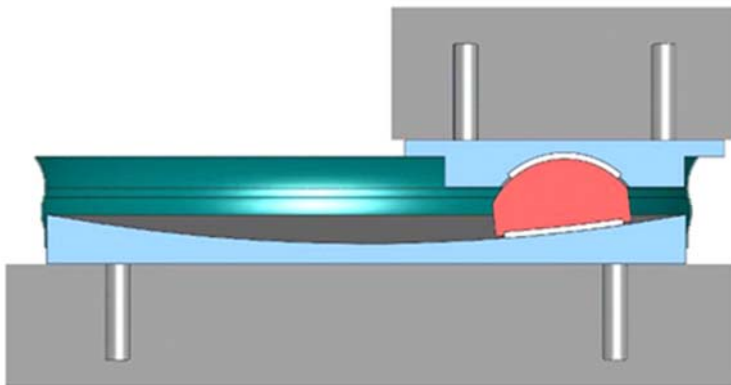
Table 11 Seismic acceleration (m/s^2) at the breakaway (average value \pm standard deviation over the set of seven ground motions)

limit state	friction model			
	<i>VelDependent</i>	<i>VC</i>	<i>VNC</i>	<i>BVNC</i>
<u><i>DLS</i></u>	0.472 ± 0.274	0.472 ± 0.274	0.472 ± 0.274	NA (*)
<u><i>CLS</i></u>	0.317 ± 0.179	0.317 ± 0.179	0.317 ± 0.179	1.016 ± 0.568

(*) Not Applicable, activation of sliding isolators occurring only for 3 out of 7 ground motion inputs



(a)



(b)

Fig. 1 Sketch of the single Curved Surface slider, or single Friction Pendulum bearing: (a) undeformed configuration; (b) deformed configuration

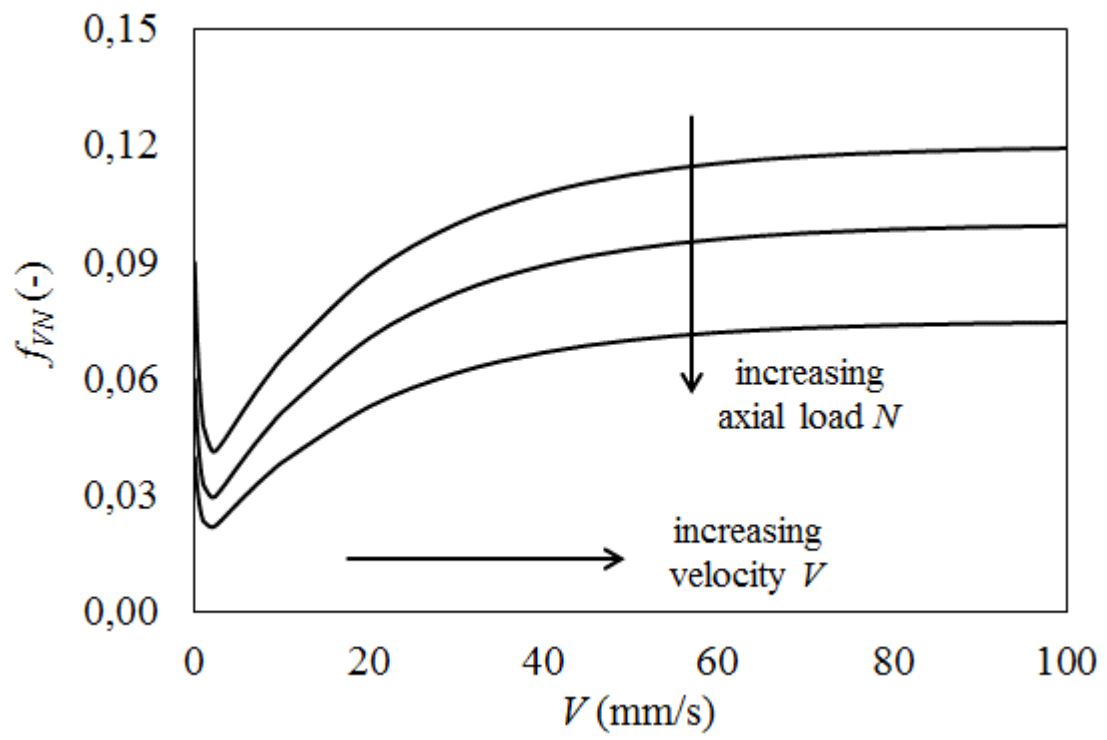


Fig. 2 Variation of coefficient of friction induced by sliding velocity and axial load

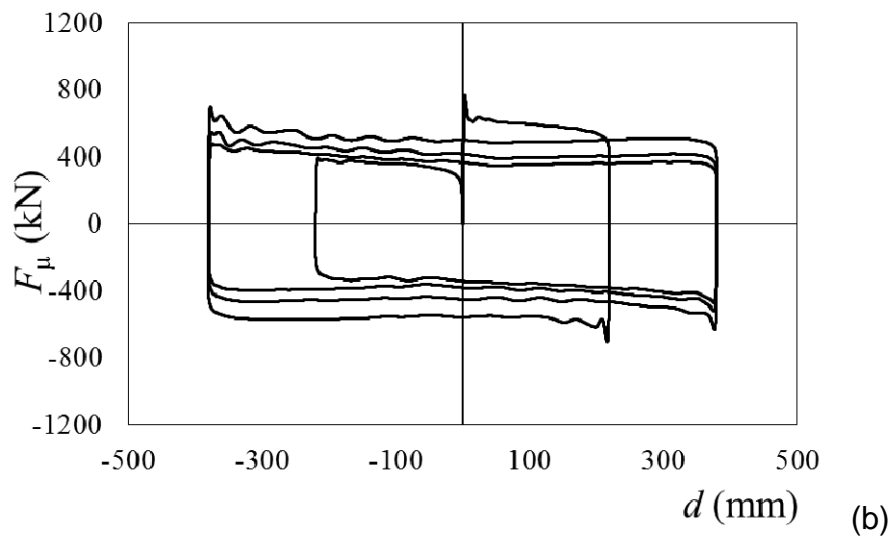
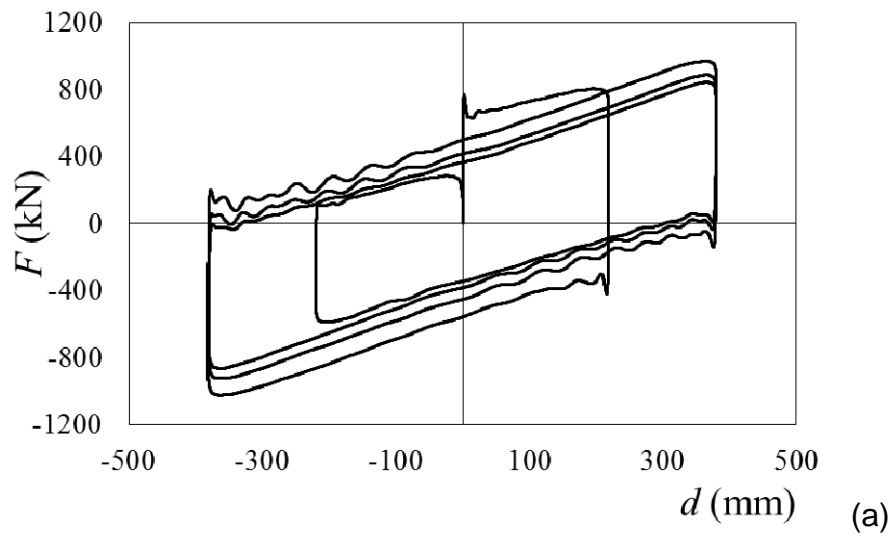


Fig. 3. Unidirectional cyclic test on CSS isolator: (a) experimental force – displacement curve; (b) calculated hysteretic (friction) force – displacement diagram

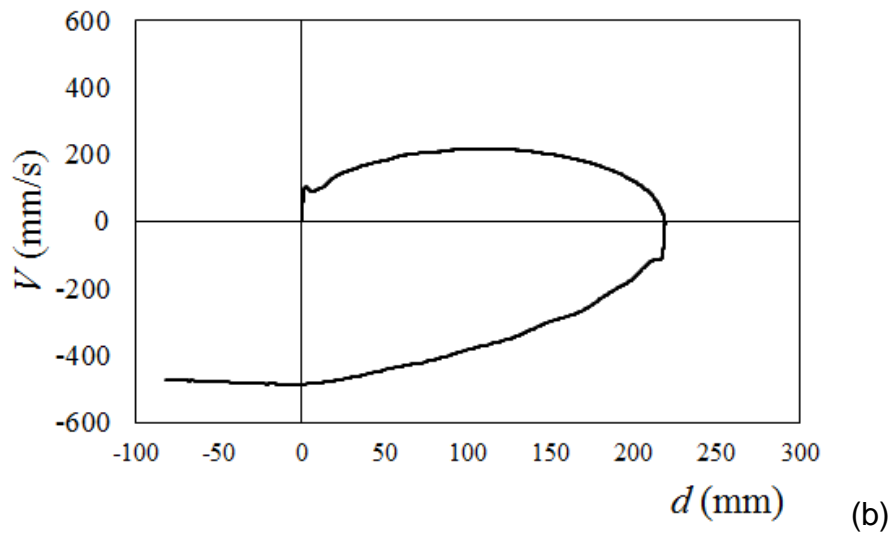
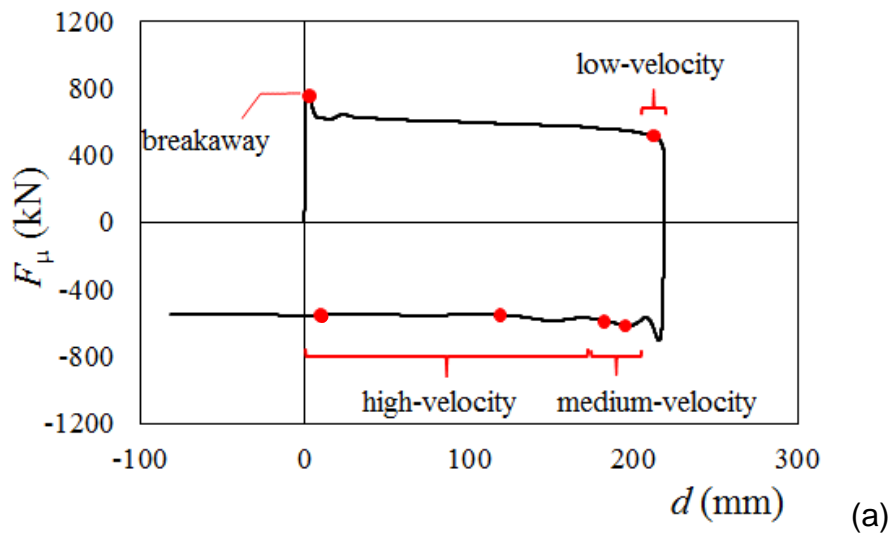


Fig. 4 (a) Values of hysteretic force sampled from the initial half cycle, and (b) associated velocity profile

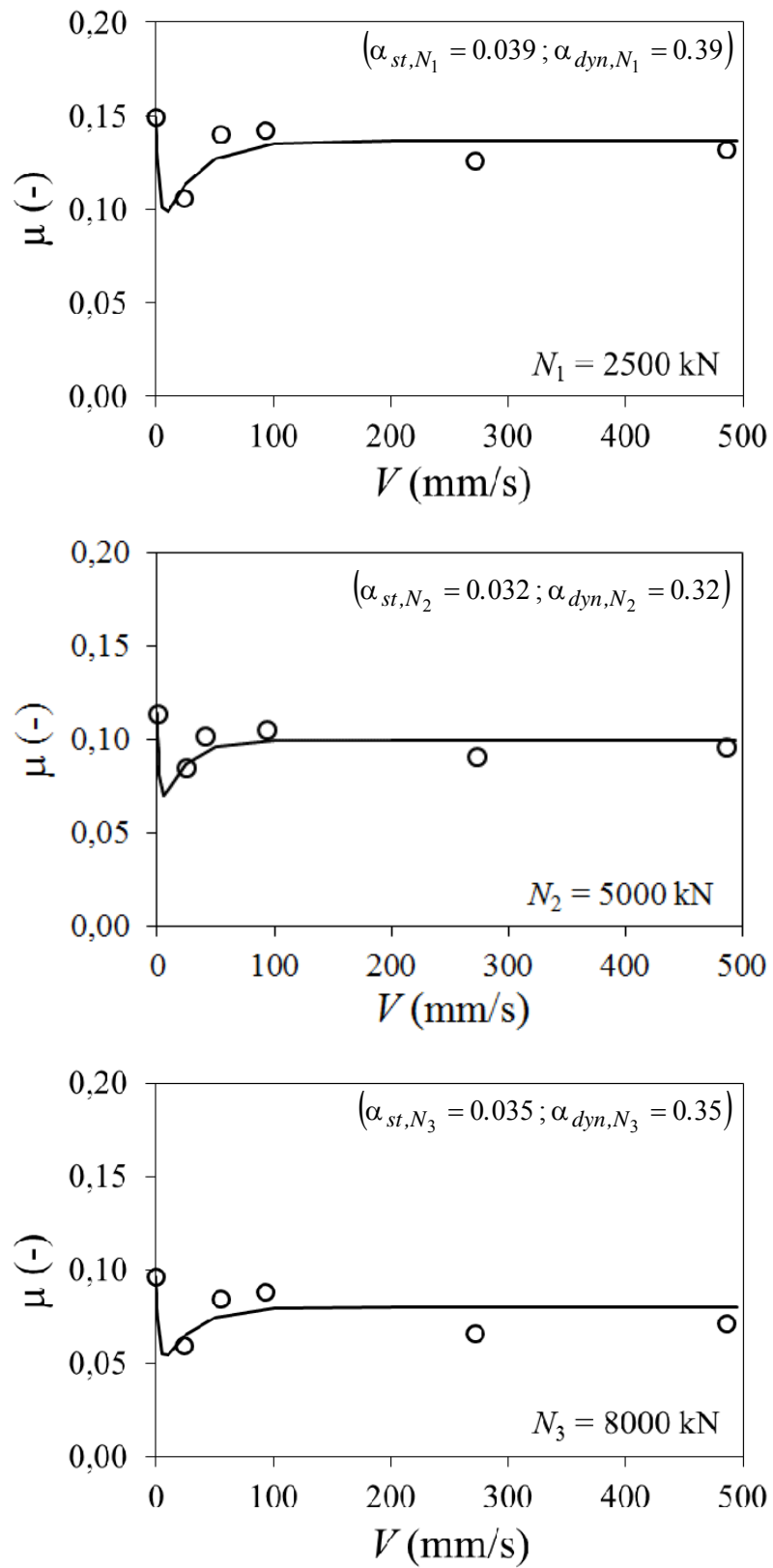


Fig. 5 Least-square fitting of experimental (μ, V) data points in accordance with Eq. (6). Load sensitive parameters α_{st, N_i} and α_{dyn, N_i} are given in brackets for each load level

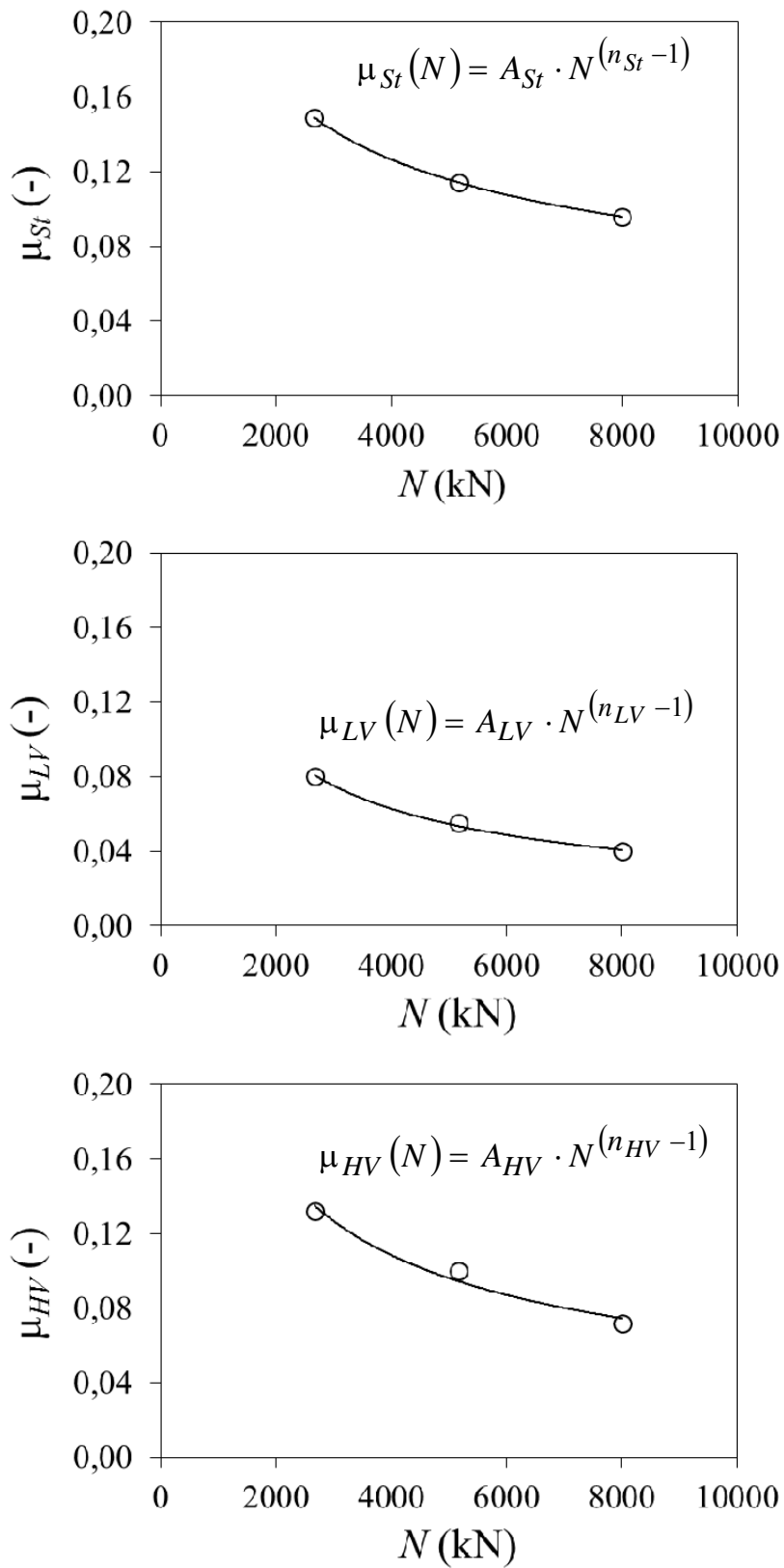
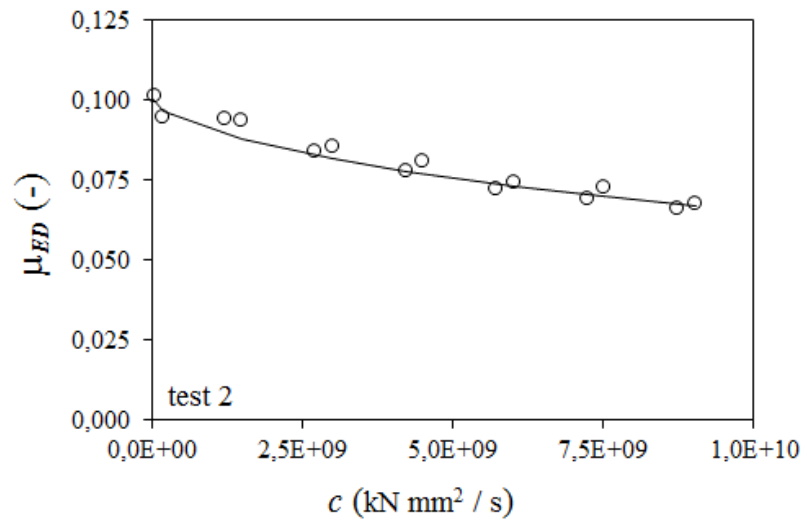
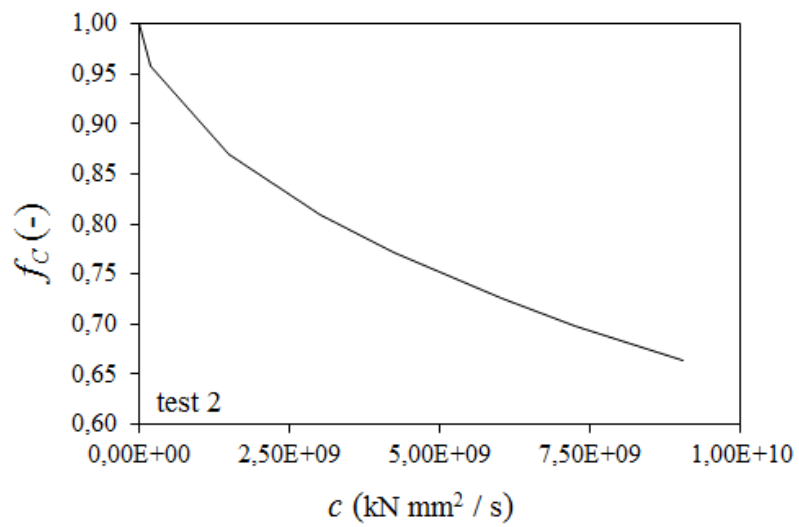


Fig. 6 Variation of friction coefficients μ_{HV} , μ_{LV} , μ_{St} with axial load and determination of model parameters A_{St} , n_{St} , A_{LV} , n_{LV} , A_{HV} , n_{HV} from curve-fitting in accordance with Eq. (7a-c)



(a)



(b)

Fig. 7 (a) Equivalent coefficient of friction and (b) degradation function vs. degradation variable c during test 2 at maximum seismic load $N_2 = 5000$ kN

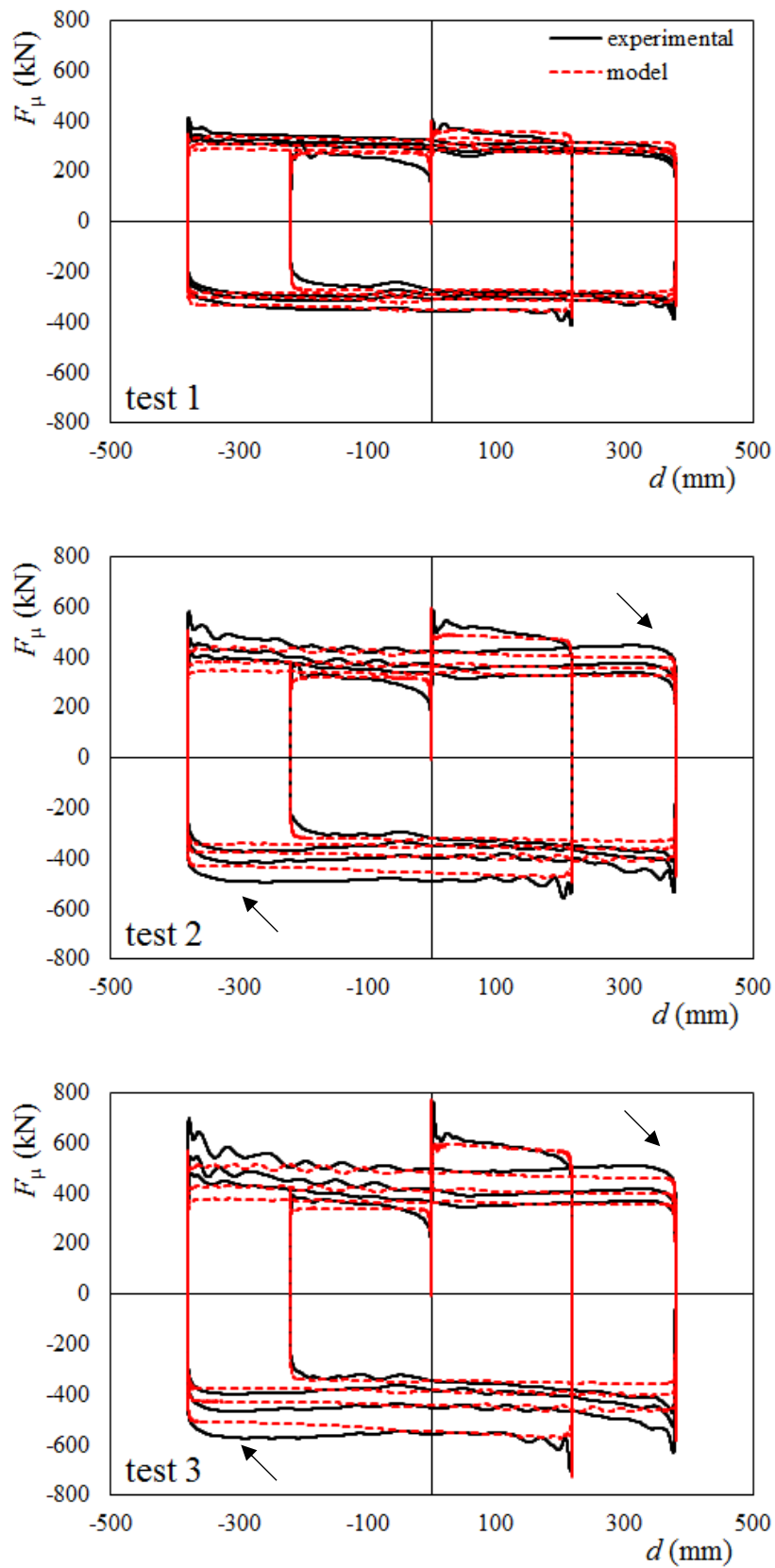
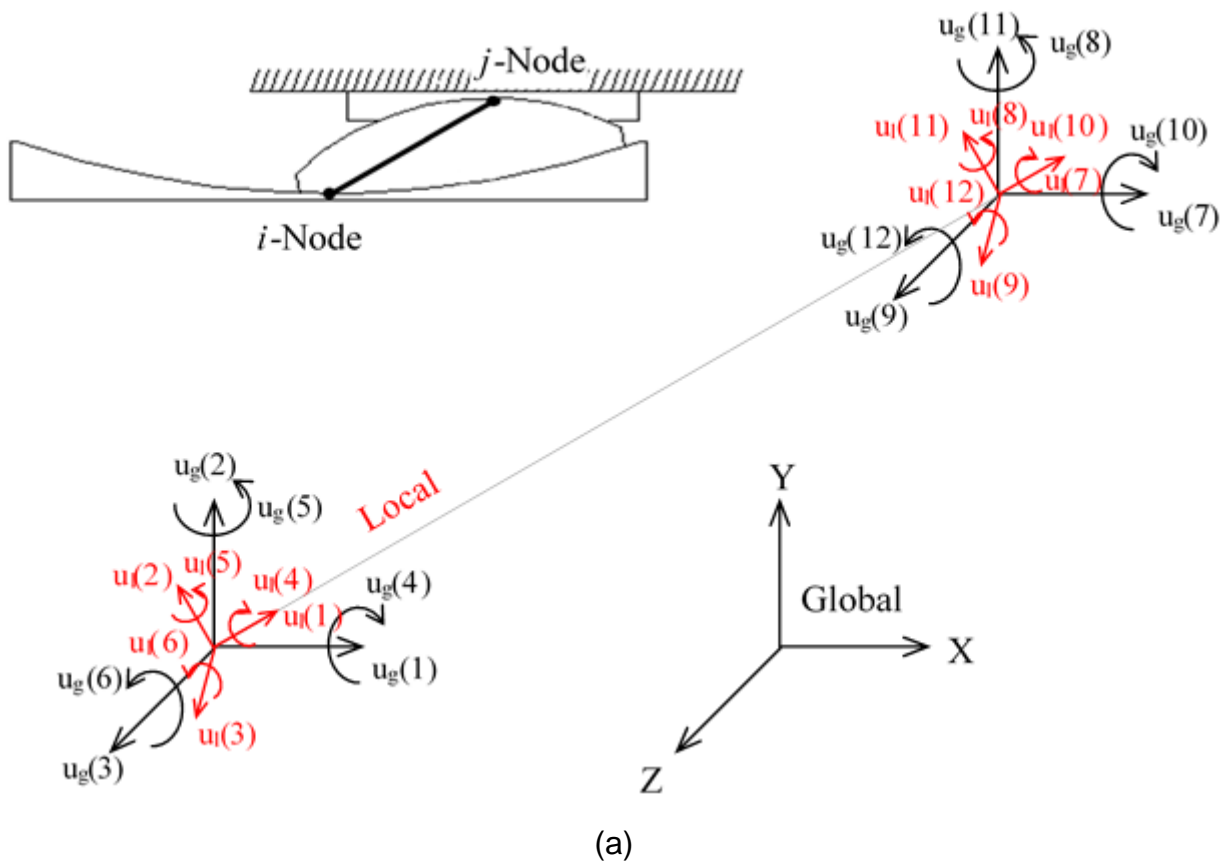


Fig. 8 Comparison between experimental (solid curves) and numerical (dotted curves) hysteretic force – displacement loops at three load levels



(a)

Fig. 9 Coordinate systems used in OpenSees: (a) global and local coordinate systems; (b) basic coordinate system. In the basic system, the kinematics of the element follows the kinematics of a pendulum with pivot point in the C -Node and length equal to R (effective radius of the bearing)

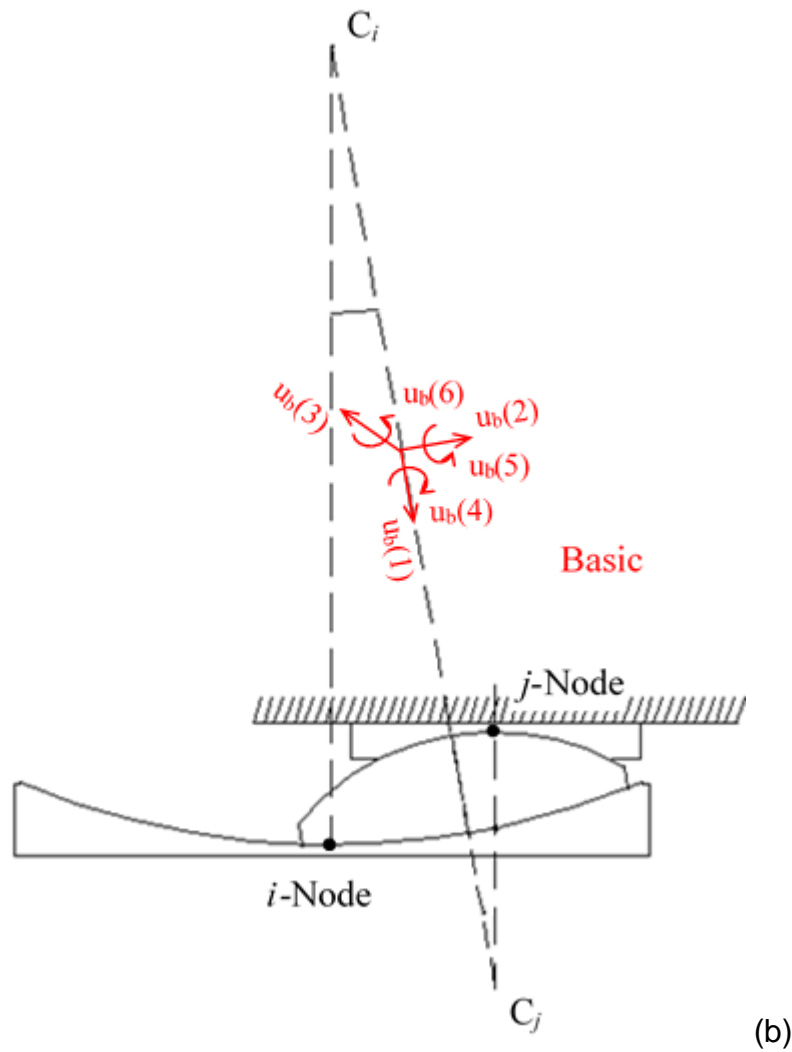


Fig. 9 Coordinate systems used in OpenSees: (a) global and local coordinate systems; (b) basic coordinate system. In the basic system, the kinematics of the element follows the kinematics of a pendulum with pivot point in the C_i -Node and length equal to R (effective radius of the bearing)

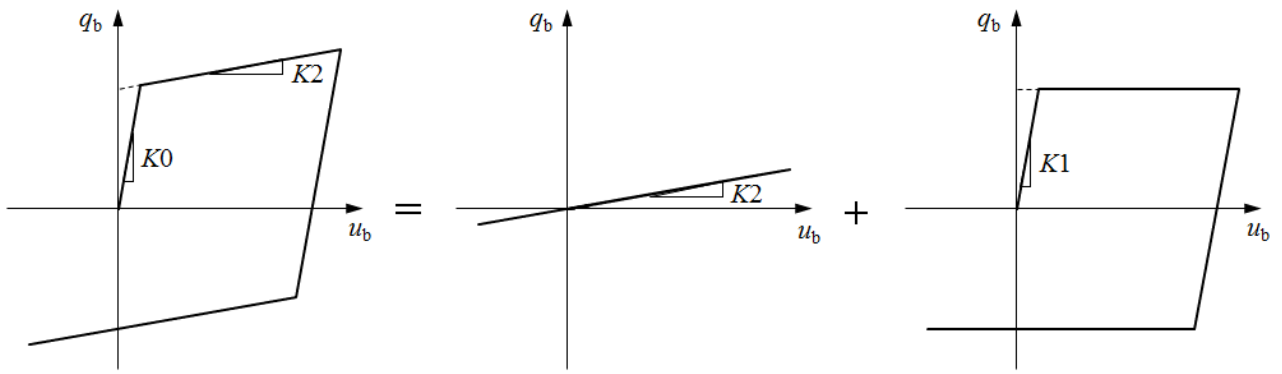


Fig. 10 Elastic and hysteretic resisting force components in the plasticity model [32]

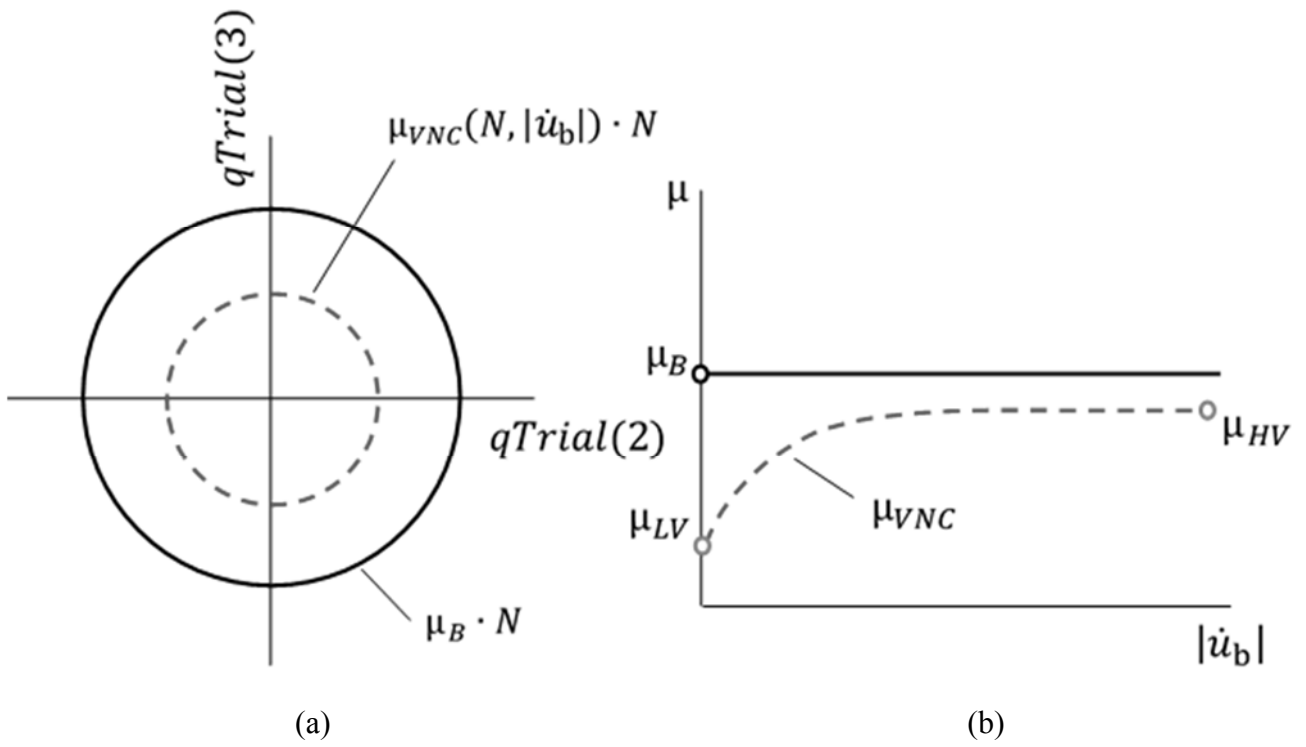


Fig. 11 (a) Bidirectional plasticity domain and (b) associated friction models

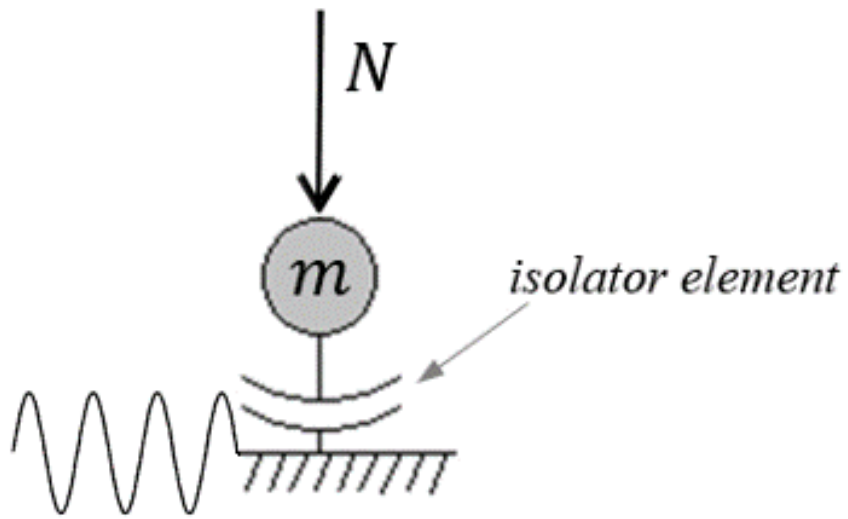


Fig. 12 SDOF model for code verification tests

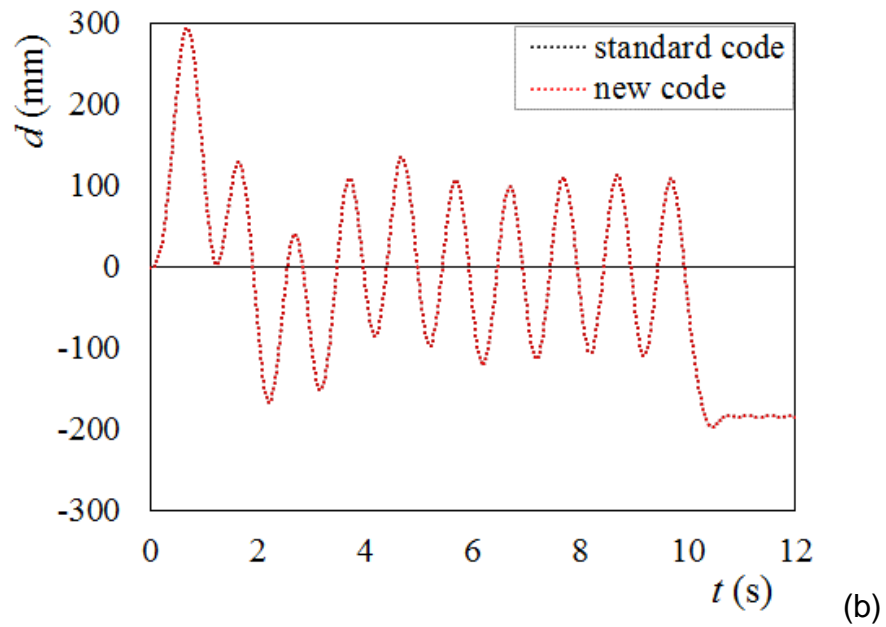
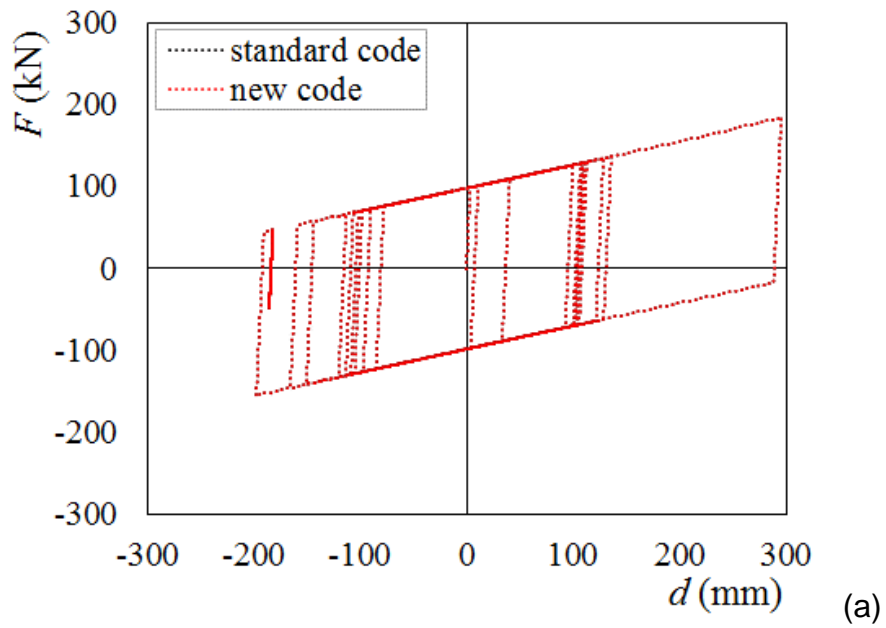


Fig. 13 Code-to-code comparison between the *CSSBearingBVNC* element (new code) and the *SingleFPSimple3D* element (standard code) with assigned *Coulomb* friction model

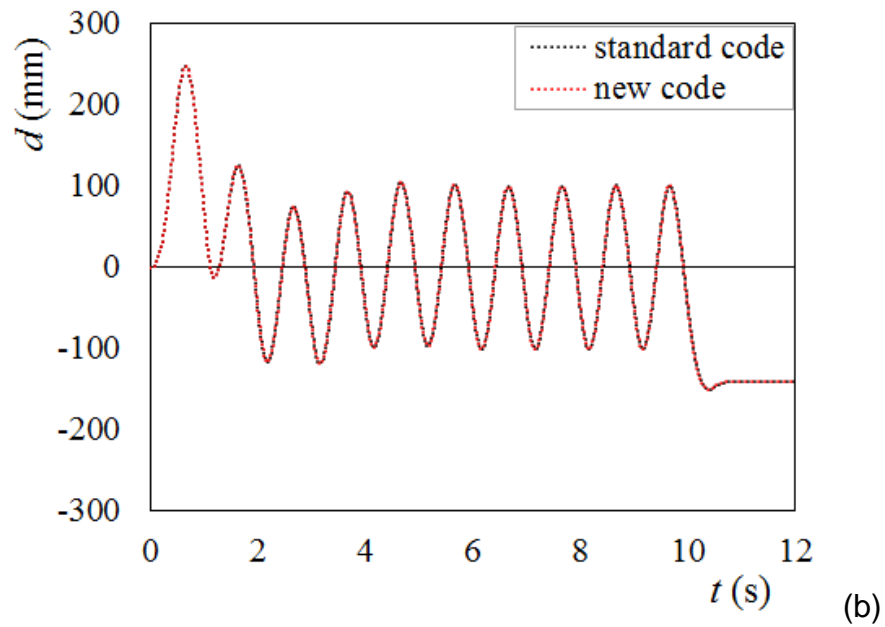
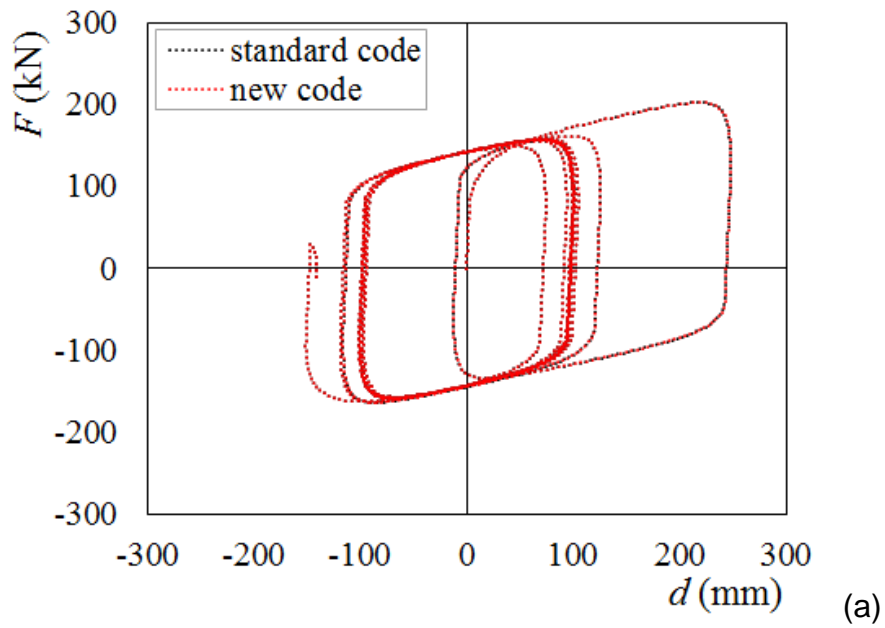


Fig. 14 Code-to-code comparison between the *CSSBearingBVNC* element (new code) and the *SingleFPSimple3D* element (standard code) with assigned *VelDependent* friction model

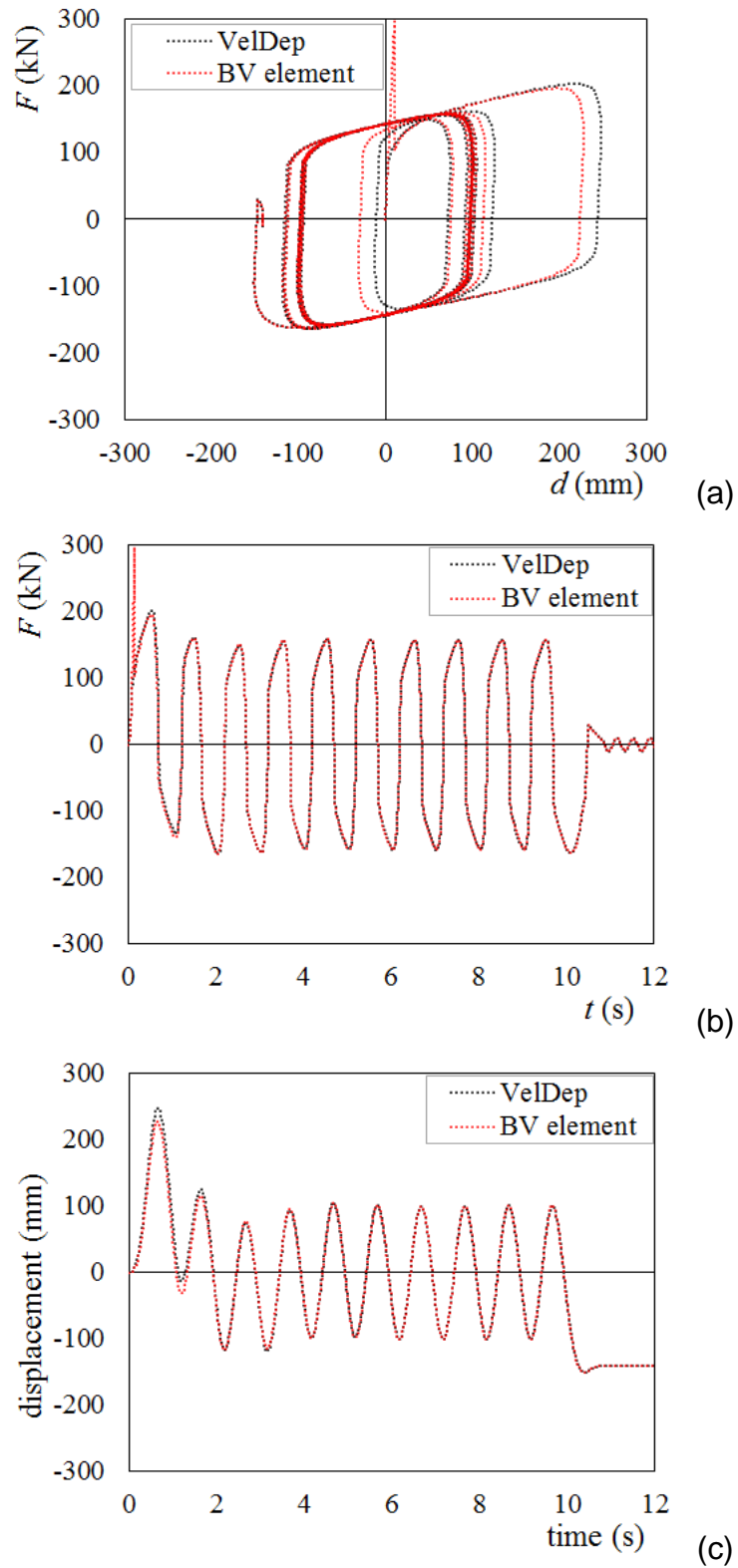


Fig. 15 Code-to-code comparison between the *CSS Bearing BVNC* element accounting for velocity and static friction effects (BV element) and the standard element with assigned *VelDependent* friction model (VelDep)

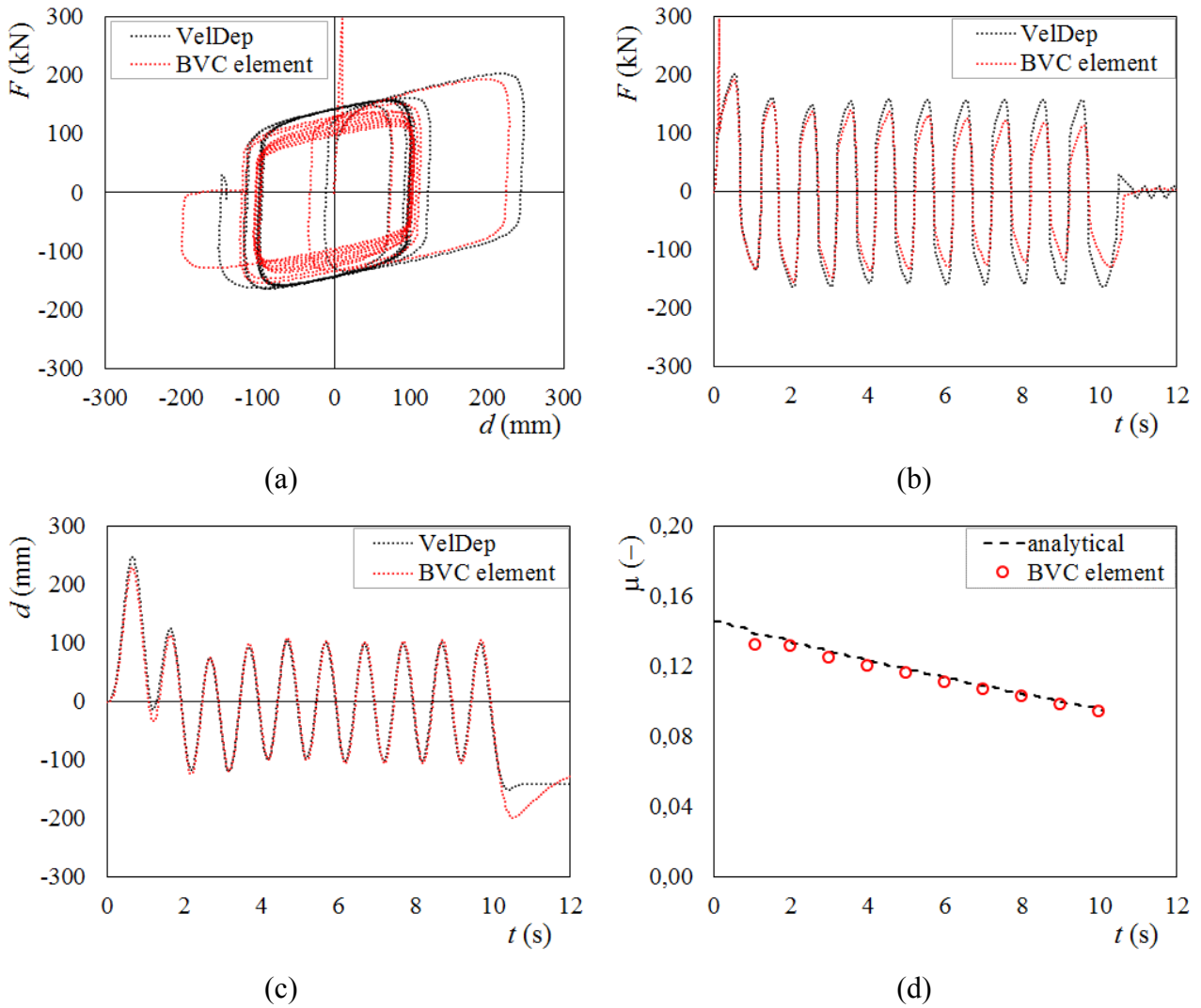


Fig. 16 Code-to-code comparison (a-c) between the *CSSBearingBVNC* element accounting for velocity, static friction and thermal effects (BVC element) and the standard element with assigned *VelDependent* friction model (VelDep); (d) decrease of the coefficient of friction compared to the analytical solution according to Eq. (8)

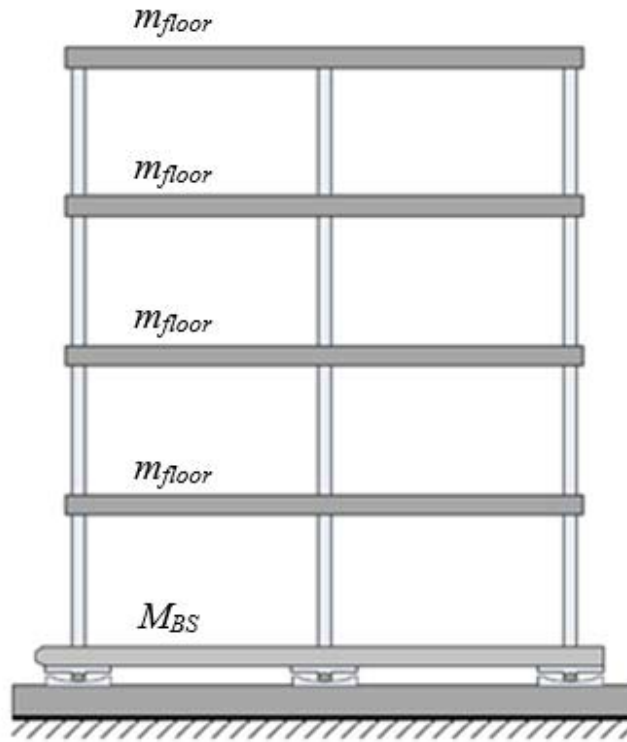


Fig. 17 Section of the case-study building, base-isolated with CSS units, where m_{floor} is the mass of each floor and M_{BS} is the mass of the base slab

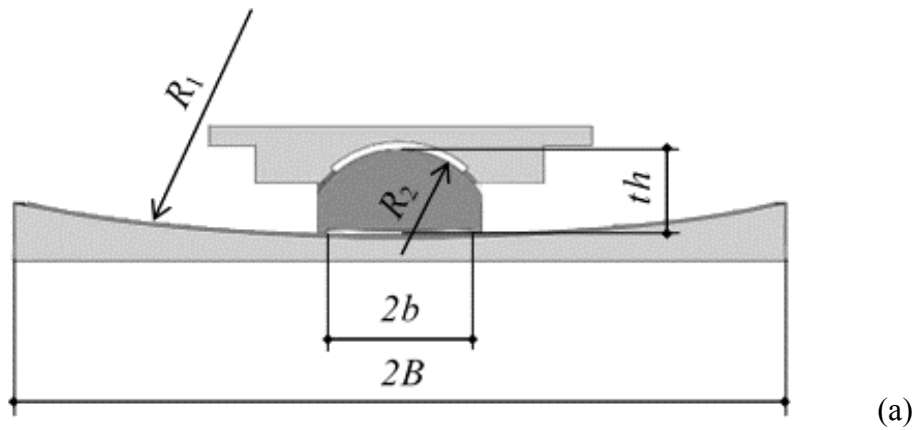


Fig. 18 CSS isolator examined in the case study: (a) geometric parameters: radius of concave sliding surface $R_1 = 2750$ mm; radius of spherical articulation $R_2 = 310$ mm; slider thickness $th = 60$ mm; diameter of contact area between slider and concave surface $2b = 170$ mm; diameter of the horizontal projection of the concave surface $2B = 470$ mm; (b) reference coefficient of friction at different velocities and load levels; (c) horizontal force – displacement curve at 555 kN axial load for sinusoidal displacement input

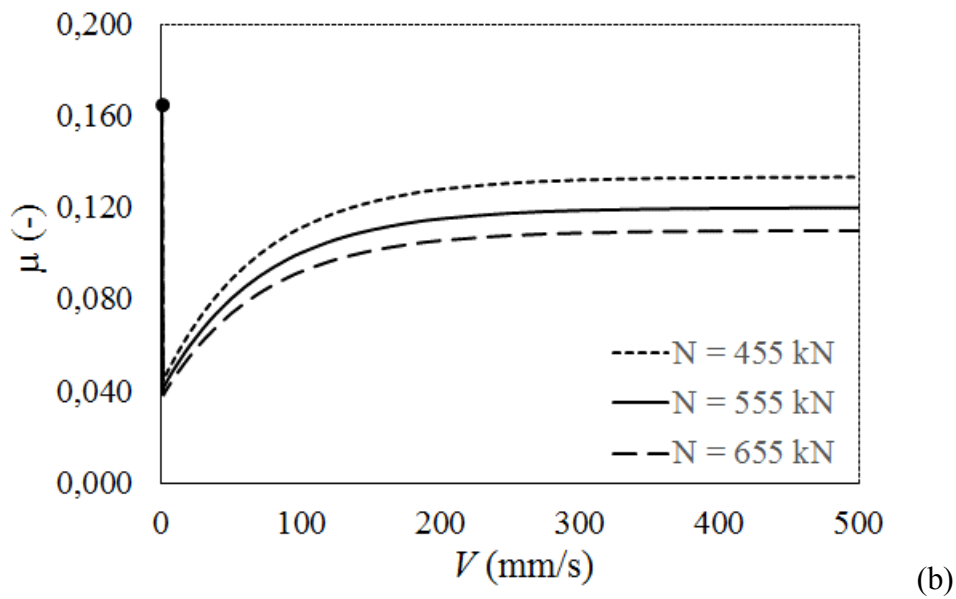


Fig. 18 CSS isolator examined in the case study: (a) geometric parameters: radius of concave sliding surface $R_1 = 2750$ mm; radius of spherical articulation $R_2 = 310$ mm; slider thickness $th = 60$ mm; diameter of contact area between slider and concave surface $2b = 170$ mm; diameter of the horizontal projection of the concave surface $2B = 470$ mm; (b) reference coefficient of friction at different velocities and load levels; (c) horizontal force – displacement curve at 555 kN axial load for sinusoidal displacement input

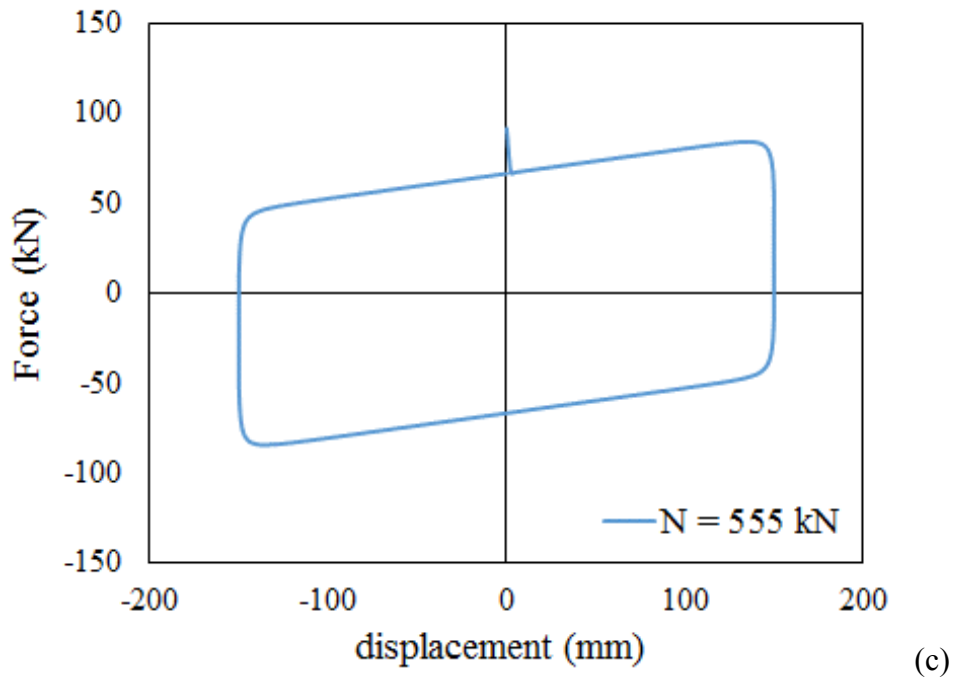


Fig. 18 CSS isolator examined in the case study: (a) geometric parameters: radius of concave sliding surface $R_1 = 2750$ mm; radius of spherical articulation $R_2 = 310$ mm; slider thickness $th = 60$ mm; diameter of contact area between slider and concave surface $2b = 170$ mm; diameter of the horizontal projection of the concave surface $2B = 470$ mm; (b) reference coefficient of friction at different velocities and load levels; (c) horizontal force – displacement curve at 555 kN axial load for sinusoidal displacement input

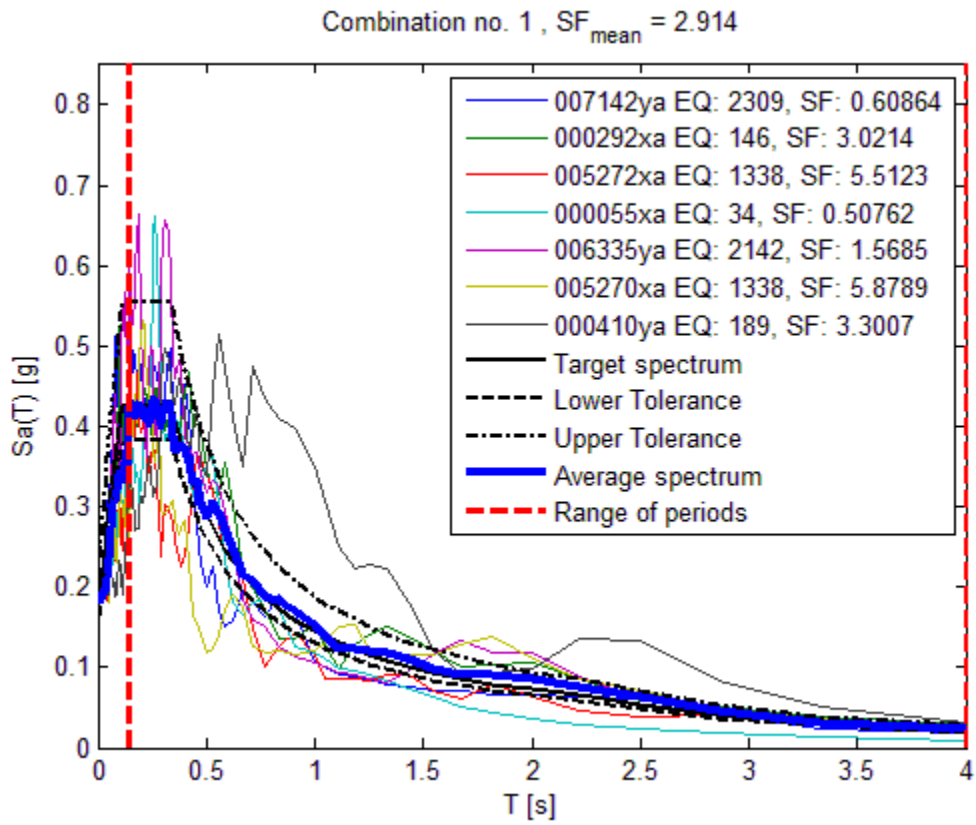


Fig. 19 Scaled ground motion acceleration spectra and target spectrum according to the Italian Building Code ($\xi = 5\%$) at DLS level

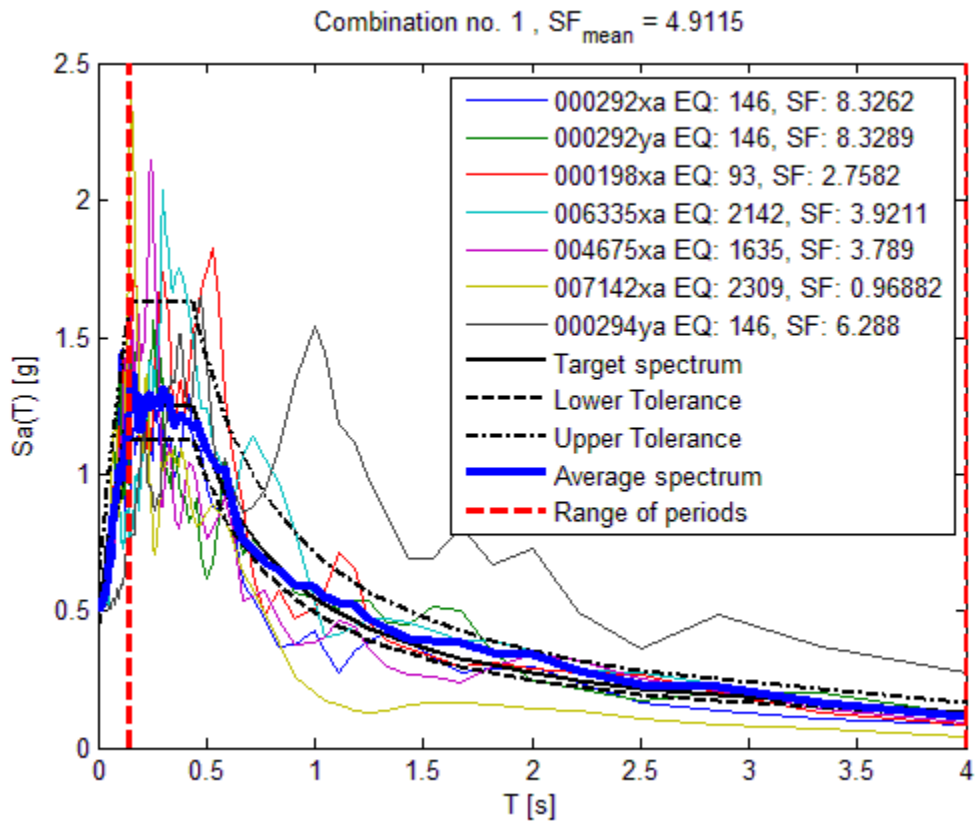


Fig. 20 Scaled ground motion acceleration spectra and target spectrum according to the Italian Building Code ($\xi = 5\%$) at CLS level

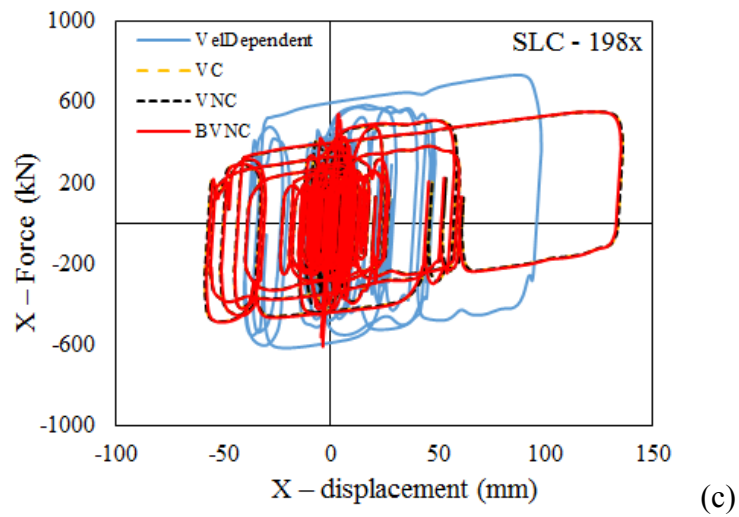
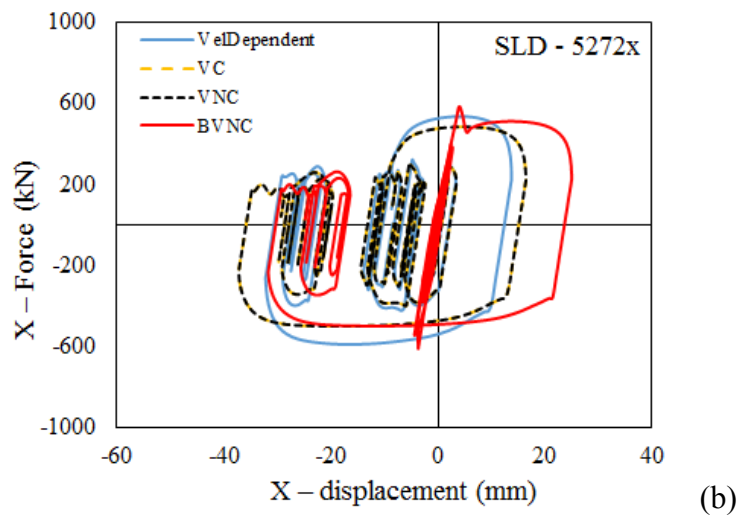
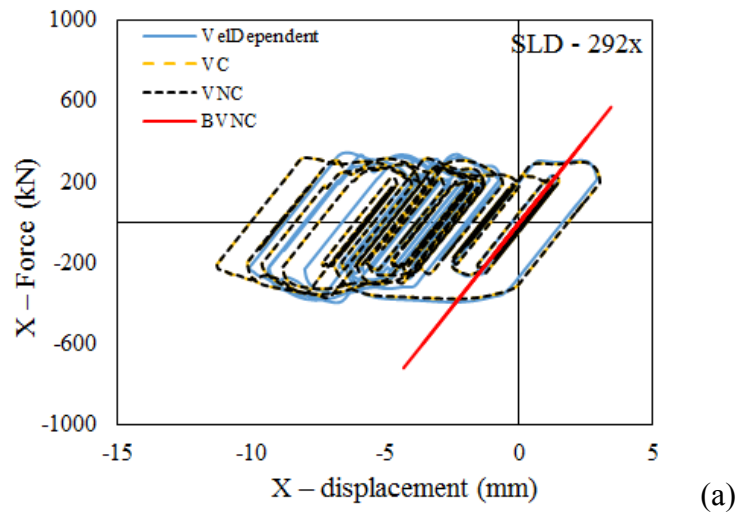


Fig. 21 Overall shear force vs. horizontal displacement of the isolation system: (a) DLS level, 292x record; (b) DLS level, 5272x record; (c) CLS level, 198x record

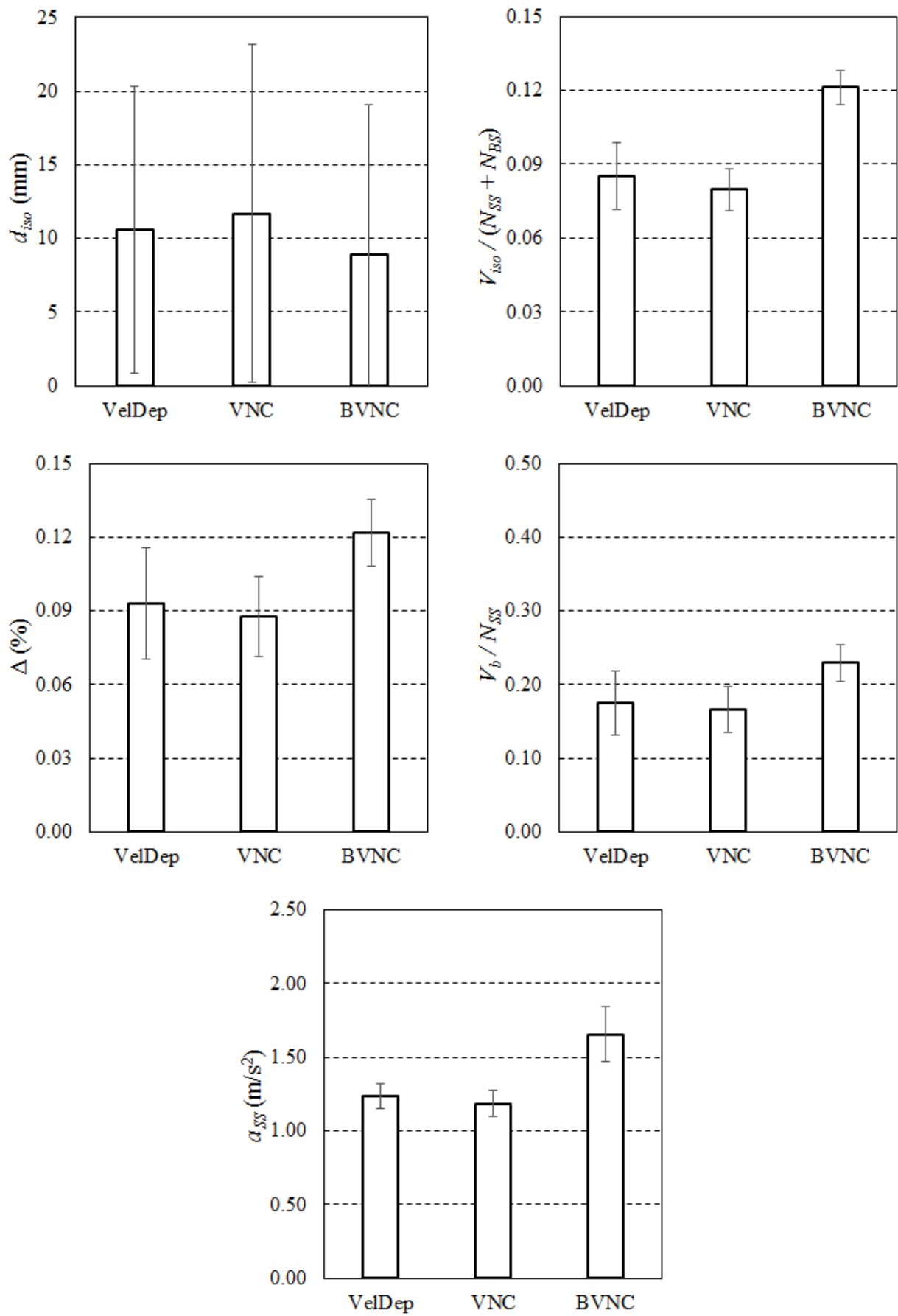


Fig. 22 Response of the base-isolated structure at DLS level

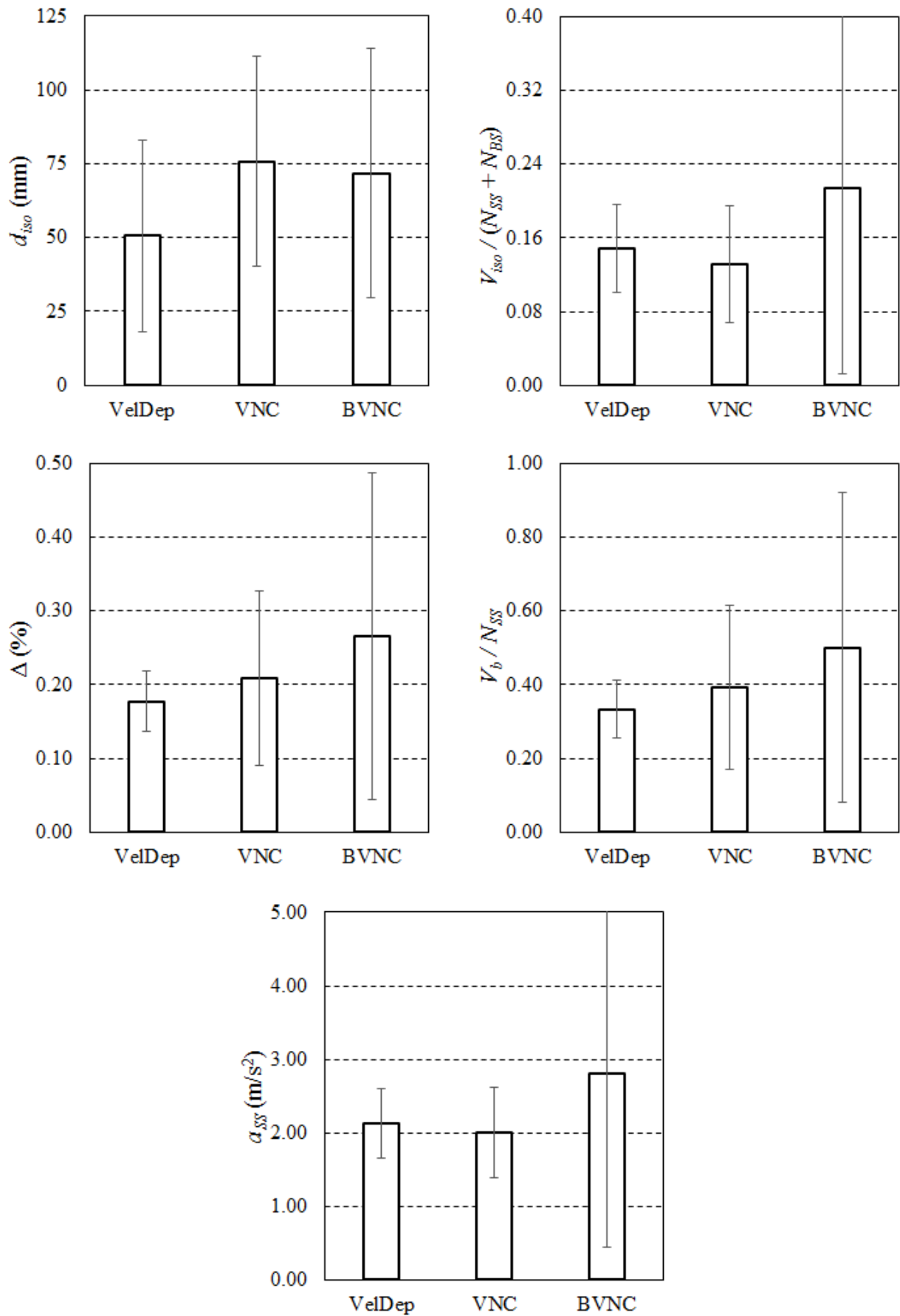


Fig. 23 Response of the base-isolated structure at CLS level

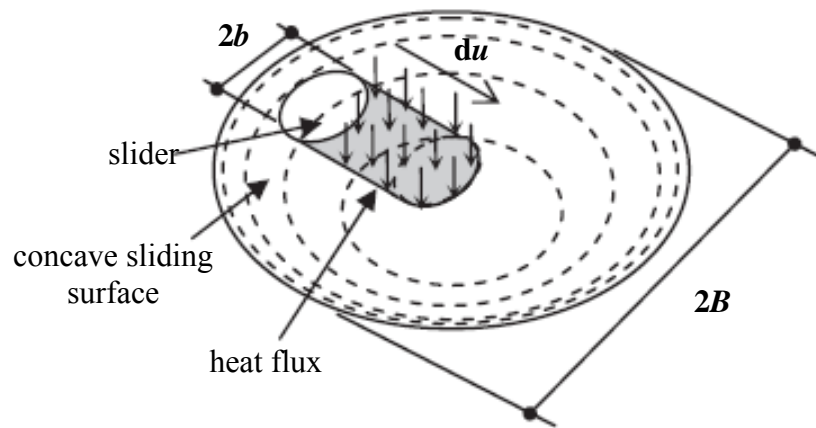


Fig. A1 Heat flux generated by the moving slider and supplied to the concave sliding surface in the time interval dt (from [19])

MOX Technical Reports, last issues

Dipartimento di Matematica
Politecnico di Milano, Via Bonardi 9 - 20133 Milano (Italy)

- 11/2018** Delpopolo Carciopolo L.; Bonaventura L.; Scotti A.; Formaggia L.
A conservative implicit multirate method for hyperbolic problems
- 12/2018** Dal Santo, N.; Deparis, S.; Manzoni, A.; Quarteroni, A.
Multi space reduced basis preconditioners for large-scale parametrized PDEs
- 09/2018** Menafoglio, A.; Grasso, M.; Secchi, P.; Colosimo, B.M.
Profile Monitoring of Probability Density Functions via Simplicial Functional PCA with application to Image Data
- 10/2018** Menafoglio, A.; Gaetani, G.; Secchi, P.
Random Domain Decompositions for object-oriented Kriging over complex domains
- 08/2018** Bonaventura, L.; Casella, F.; Delpopolo, L.; Ranade, A.;
A self adjusting multirate algorithm based on the TR-BDF2 method
- 06/2018** Antonietti, P.F.; Mazzieri, I.
High-order Discontinuous Galerkin methods for the elastodynamics equation on polygonal and polyhedral meshes
- 07/2018** Ieva, F.; Bitonti, D.
Network Analysis of Comorbidity Patterns in Heart Failure Patients using Administrative Data
- 05/2018** Pagani, S.; Manzoni, A.; Quarteroni, A.
Numerical approximation of parametrized problems in cardiac electrophysiology by a local reduced basis method
- 03/2018** Antonietti, P. F.; Houston, P.; Pennesi, G.
Fast numerical integration on polytopic meshes with applications to discontinuous Galerkin finite element methods
- 04/2018** Ekin, T.; Ieva, F.; Ruggeri, F.; Soyer, R.
Statistical Medical Fraud Assessment: Exposition to an Emerging Field